Physikalisch Technische Bundesanstalt

Laborbericht

Milos Tichy[1], Horst Klein[2] and Jaroslav Pulpan[1]

Calibration of an NE-213 Scintillator

→ PTB-7.2-92-1
Braunschweig, July 1992

PTB

Physikalisch-Technische Bundesanstalt, Braunschweig und Berlin

Die Physikalisch-Technische Bundesanstalt (PTB) ist das natur- und ingenieurwissenschaftliche Staatsinstitut und zugleich die technische Oberbehörde für das Meßwesen im Dienstbereich des Bundesministers für Wirtschaft. Sie beschäftigt etwa 2000 Mitarbeiter, davon über ein Viertel mit Hochschulbildung, die in 23 allgemeinen Referaten und mehr als 120 Laboratorien in 10 Abteilungen in Braunschweig (Mechanik und Akustik, Elektrizität, Thermodynamik, Optik, Fertigungsmeßtechnk, Atomphysik, Neutronenphysik, Technisch-Wissenschaftliche Dienste) und Berlin (Temperatur und Synchrotronstrahlung, Medizinphysik und Informationstechnik) der PTB tätig sind.

Aufgaben der Bundesanstalt

Physikalische und ingenieurwissenschaftliche Forschung – Präzisionsbestimmung physikalischer Konstanten – Realisierung und Weitergabe der SI-Einheiten – Darstellung und Verbreitung der Gesetzlichen Zeit – Darstelllung der Internationalen Temperaturskala – Bauartprüfung, Zulassung und Kalibrierung von Meßeinrichtungen, Spielgeräten und zivilen Schußwaffen – Bauartprüfung auf dem Gebiet der Sicherheitstechnik, des Strahlenschutzes, der Heilkunde und der Überwachung des Straßenverkehrs – Auftragsprüfung und Industrieunterstützung durch wissenschaftlich-technische Beratung – Bestätigung und Überwachung der Kalibrierlaboratorien des Deutschen Kalibrierdienstes (DKD) – Ausarbeitung technischer Vorschriften und Richtlinien – Mitwirkung in nationalen und internationalen Fachgremien – Meßtechnische Bildungs- und Entwicklungshilfe.

Veröffentlichungen

- PTB-Mitteilungen (zweimonatlich erscheinendes wissenschaftliches und amtliches Fachorgan der PTB)
- Jahresbericht der PTB (erscheint im Frühjahr des folgenden Jahres)
- PTB-Berichte (als Manuskript gedruckte Einzelarbeiten; sie erscheinen nach Fachgebieten geordnet in mehreren Serien)
- PTB-Prüfregeln (Regeln für die Prüfung von Meßgeräten und Betriebsmitteln mit Beschreibung der Prüfverfahren)
- Eichanweisung (allgemeine Verwaltungsvorschriften für die Eichung von Meßgeräten)
- Eichordnung (technische Rechtsvorschriften für die Eichung von Meßgeräten)
- Technische Richtlinien (Informationen und Empfehlungen für die staatlich anerkannten Prüfstellen für Meßgeräte)
- Verzeichnis der Kalibrierlaboratorien, Richtlinien und Jahresberichte des Deutschen Kalibrierdienstes (DKD)
- SI-Basiseinheiten (Definition, Entwicklung, Realisierung)
- Informationsbroschüren, Presse-Informationen

The Physikalisch-Technische Bundesanstalt (PTB) is the national institute for science and technology and the highest technical authority for metrology under the auspices of the Federal Minister of Economics. It has approx. 2 000 employees, more than a quarter of whom have a university education. The PTB consists of 23 general administrative sections and more than 120 laboratories divided into 10 divisions in Braunschweig (Mechanics and Acoustics; Electricity; Thermodynamics; Optics; Precision Engineering; Atomic Physics; Neutron Physics; Technical and Scientific Services) and Berlin (Temperature and Synchrotron Radiation; Medical Physics and Information Technology).

Tasks of the Bundesanstalt

Research in the fields of physics and technology – Precise determination of physical constants – Realization and dissemination of the SI units – Realization and propagation of legal time – Realization of the International Temperature Scale – Pattern evaluation, pattern approval and calibration of measuring instruments, gambling devices and civil fire-arms – Pattern evaluation in the fields of safety technology, radiation protection, medicine and traffic control – Test work on commission and assistance to industry by consultancy services in science and technology – Accreditation and supervision of the calibrating laboratories of the German Calibration Service (DKD) – Drawing-up of technical regulations and directives – Cooperation in national and international technical committees – Educational and development aid in the field of metrology.

Publications

- PTB Communications (Scientific official publication of the PTB, issued bimonthly)
- PTB Annual Report (Published in spring of the following year)
- PTB Reports (Scientific papers printed in manuscript form. They are published in several series classified according to subject)
- PTB Testing Instructions (Instructions for the testing of measuring instruments and working equipment with a description of the testing procedures)
- Verification Instructions (Publication of general administrative regulations for the verification of measuring instruments)
- Verification Ordinance (Publication of legal technical regulations for the verification of measuring instruments)
- Technical Directives (Information and recommendations for the state-approved test centres for measuring instruments)
- List of calibrating laboratories, directives and annual reports of the German Calibration Service (DKD)
- SI base units (Definition, development, realization)
- Informative brochures, Press Release

Anschriften/Adresses

Braunschweig:
Bundesallee 100, 3300 Braunschweig
Telefon: (05 31)5 92-0
Telex: 95 28 22 ptb d
Telefax: 05 31/5 92-40 06
Teletex: 5 31 82 09 ptb

Berlin-Charlottenburg:
Abbestraße 2-12, 1000 Berlin 10
Telefon: (0 30)34 81-1
Telefax: 0 30/34 81-4 90

Berlin-Friedrichshagen:
Fürstenwalder Damm 388, O-1162 Berlin
Telefon: (0 03 72)64 41-0
Telefax: 00 37-2-64 41-3 48

Empfohlene Zitierweise/recommended citation

Tichy, M., Klein, H. und J. Pulpan, 1992. *Calibration of an NE-213 Scintillator.* Braunschweig: Physikalisch-Technische Bundesanstalt. PTB-Laborbericht PTB-7.2-92-1. Verfügbar unter: https://doi.org/10.7795/130.20231025

Tichy, M., Klein, H. and J. Pulpan, 1992. *Calibration of an NE-213 Scintillator.* Braunschweig: Physikalisch-Technische Bundesanstalt. PTB-Laborbericht PTB-7.2-92-1. Available at: https://doi.org/10.7795/130.20231025

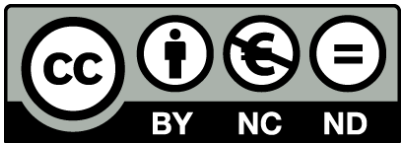

Herausgeber/editor:
Physikalisch-Technische Bundesanstalt
ISNI: 0000 0001 2186 1887

Presse und Öffentlichkeitsarbeit

Bundesallee 100
38116 Braunschweig

Telefon: (05 31) 592-93 21
Telefax: (05 31) 592-92 92
www.ptb.de

Physikalisch-Technische Bundesanstalt

Abteilung Neutronenphysik

Laborbericht PTB-7.2-92-1

Calibration of an NE-213 Scintillator

by

Milos Tichy[1], Horst Klein[2] and Jaroslav Pulpan[1]

[1] Institute of Radiation Dosimetry,
Na Truhlarce 39, 180 86 Prague 8, Czechoslovakia

[2] Physikalisch-Technische Bundesanstalt,
Bundesallee 100, W-3300 Braunschweig

https://doi.org/10.7795/130.20231025

https://doi.org/10.7795/130.20231025

Abstract

A complete calibration of an NE213 liquid scintillation detector, 5.08 cm (2") in diameter and 5.08 cm in length, was performed at the PTB accelerator facility. The light output functions of the secondary charged particles and the resolution parameters were determined by measuring the response for 33 neutron energies between 1 MeV and 16 MeV taking advantage of the time-of-flight technique. The response functions were than simulated with the NRESP7 code on the basis of these parameters and showed good agreement with the measured spectra. The neutron fluences resulting from these comparisons reasonably agreed with the data measured with the calibrated reference detector of PTB. The calculated neutron detection efficiencies and response matrix were than used to normalize the time-of-flight spectra of broad neutron energy distributions and to unfold the simultaneously taken pulse height spectra respectively. The very good agreement of both spectral fluences in the entire energy range finally confirmed the unfolding procedure DIFBAS.

Zusammenfassung

Ein für die Spektrometrie schneller Neutronen eingesetzter flüssiger Szintillator NE213, 5.08 cm (2") im Durchmesser und 5.08 cm lang, wurde an der Beschleunigeranlage der PTB kalibriert. Die Lichtausbeutefunktionen der sekundären geladenen Teilchen und die Auflöseparameter konnten bestimmt werden, indem unter Verwendung der Flugzeittechnik die Antwortfunktionen für 33 Neutronenenergien zwischen 1 MeV und 16 MeV gemessen wurden. Auf der Basis dieser Parameter wurden dann die Antwortfunktionen mit dem Simulationsprogramm NRESP7 berechnet. Der Vergleich mit den Messungen ergab eine gute Übereinstimmung in der Form der Spektren. Die dabei ermittelten Neutronenfluenzen stimmten ebenfalls gut mit den Vergleichsdaten eines kalibrierten Referenzdetektors der PTB überein. Die berechneten Nachweis-wahrscheinlichkeiten und Antwortfunktionen wurden dann für die Normierung von Flugzeitspektren breiter Neutronenenergie-verteilungen bzw. die Entfaltung der gleichzeitig gemessenen Pulshöhenspektren verwendet. Die sehr gute Übereinstimmung der beiden spektralen Fluenzen über den gesamten Energiebereich bestätigte schließlich das hier eingesetzte Entfaltungsverfahren DIFBAS.

https://doi.org/10.7795/130.20231025

https://doi.org/10.7795/130.20231025

Contents

https://doi.org/10.7795/130.20231025

https://doi.org/10.7795/130.20231025

1. Introduction.

Discrepancies between the real response of a NE-213 scintillator used and the Illinois response matrix [In-75] used for the unfolding appeared to be one possible reason for the differences between measured and calculated spectra in benchmarks with Fe, Ni, Al and Pb [Ti-1-90]. This error source was confirmed by the good agreement between model and unfolded spectra in DIFBAS code testing [Ti-2-90] where an inadequacy of the response matrix was excluded. Preliminary calculations of responses using the NRESP code [Di-1-82] compared with measured data have shown that the responses of NE-213 scintillators can substantially differ even if they are of the same dimensions. The problem can be solved by a precise calibration in a monoenergetic neutron beam. This was performed simultaneously for four scintillators at PTB.

The content of this report is a description of the calibration and evaluation procedures for one detector (referred as the IRD detector). The chronology of the evaluation procedure is given subsequently: after a calibration with photon sources, where the scale of the ADC was set, the light output functions for protons and α particles were evaluated. After normalization and dead-time corrections, fluences were then calculated. A response matrix for 184 energies of neutrons between 0.5 and 20. MeV was calculated using the new light output function. The final proof of the calibration is a comparison of neutron spectra converted from TOF spectra and spectra gained from the unfolding of pulse height (PH) spectra using the new response matrix. At all stages of the evaluation, special attention was devoted to a comparison of the results obtained from measurements with different gains of the detector chain.

2. Experimental arrangement.

The calibration was performed at the PTB accelerator using the fast neutron time-of-flight (TOF) facility arranged for scattering

https://doi.org/10.7795/130.20231025

experiments [Br-80]. Deuteron projectiles accelerated by the PTB compact cyclotron produced neutrons in a deuterium gas target via D(d,n) and D(d,np) reactions. The detector to be studied was placed at a 12 m distance from the gas target in the collimated neutron beam at an angle of 0° to the deuteron beam. The neutron yield was monitored by a 1.5"*1.5" NE-213 scintillator in another collimator situated at an angle of 60.4°. Absolute normalization was assured by the irradiation of a reference detector (REF) at the same position as the detectors studied. This was also an NE-213 scintillator (4"*1") calibrated by means of a proton recoil telescope [Bo-88,Si-85].

Two sources of background radiation can be generally taken into account under the irradiation conditions used:

- scattered neutrons (on walls, ground, air);
- neutrons generated by reactions other than desired.

In the present experiment no corrections on background neutrons were taken into account during the evaluation of the measured spectra because:

- neither source has any influence on light output function evaluation, as TOF windows were used to select monoenergetic neutrons,
- the collimator was designed to minimize the influence of scattered neutrons [Sh-80] and
- the determination of the neutron yield was not the aim of this calibration procedure ("gas out" irradiation, with which the second background source can be subtracted, was therefore performed for the REF detector only).

The IRD detector is a 2"*2" NE-213 scintillator coupled via a 2.9 cm half-coated [Sc-80] lucite light guide to a photomultiplier. The light guide was used to improve the resolution at high energies and to minimize the locus dependence of the light transmission from the scintillator to the photocathode. This is the only change in the detector system described in [Pu-91]. The detector electronics system was connected to the PTB data acqui-

https://doi.org/10.7795/130.20231025

sition system [K1-80] as described on Fig. 1. The EVENT signal starts A/D conversion of PH, PS and TOF signals, producing correspondingly pulse-height (PH), pulse-shape (PS) and time-of-flight (TOF) spectra. Both EVENT and CFD rate signals were counted and the count rates used for dead-time corrections. The parameters set for all modules are listed in Appendix 1.

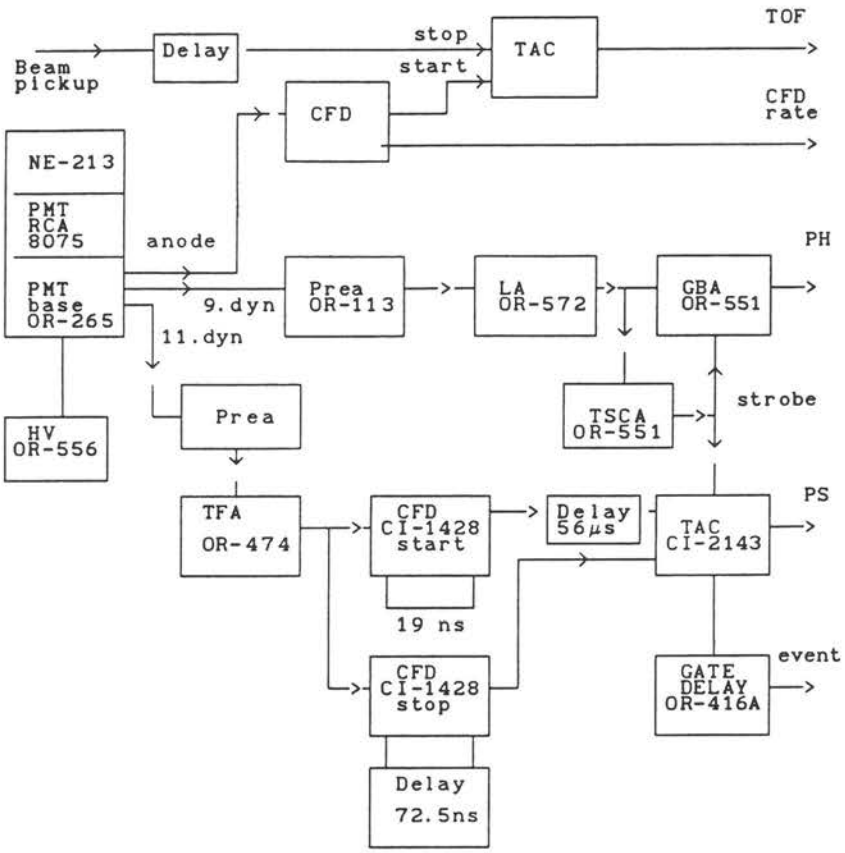

Fig. 1: Detector electronics system and its coupling to PTB data acquisition system.

https://doi.org/10.7795/130.20231025

3. Gamma calibration.

The purpose of the γ-calibration is to set up a scale for the PH spectra which can be reproduced independently on any ADC. For this purpose we established a pulse height scale in terms of light units connected to the energy of electrons, on the assumption that the light output of electrons $L_e(E)$ in the NE-213 scintillator is linear except at very low energies ($E \leq 50$ keV).

The γ-calibration was performed according to [Di-2-82]. One light unit (l.u.[1]) is defined as the light output of an electron with an energy of 1 MeV plus an offset E_o. The offset introduced in [Di-2-82] to compensate the nonlinearity of the light output for energies below 50 keV was estimated to have a value of 5 keV. This value was used in all response calculations. The calibration performed had two objectives:

- to check the assumed linearity of $L_e(E)$ and the value of the offset E_o;
- to specify the slope (or gain) G of the scale and the resolution function of the spectrometer.

The photon sources listed in Tabs. 1-5 were used for the calibration. The additional source denoted C-12 was realized by means of an Am-Be neutron source. The reaction $^{9}Be\ (\alpha,n)^{12}C$ proceeds partially via the first excited state of ^{12}C which decays by the emission of a 4.44 MeV photon. The corresponding Compton edge and double-escape peak may also be used for calibration purposes. All sources were measured separately for two gains (LGR & HGR) at distances of 10 - 40 cm from the front surface on the axis of the detector. The distance had to be varied because of the different source strengths. In all cases natural background radiation was subtracted but no shadow cone measurements were performed to subtract photons scattered on air and walls. The gain stability of the detector as a function of the count rate was checked by

---

[1] This name was chosen to avoid confusion between "proton MeV" and "electron MeV".

https://doi.org/10.7795/130.20231025

simultaneous measurements with a ^{88}Y source.

The most important point - to assign the position of the Compton edge to a measured spectrum - was solved by fitting a calculated spectrum to a measured one. Spectra for all photon energies were calculated with the GRESP code [Di-2-82] and transformed to a scale with equidistant step C [channels/keV] of the electron energy (values C = 0.070 and 0.480 were used for LGR and HGR). By means of the fitting procedure, three parameters were adjusted for each photon energy:

- the width dL/L of a Gaussian function by which the calculated spectrum had to be folded;
- the compression factor c_x by which the calculated spectrum had to be compressed or expanded;
- the count rate factor by which the calculated and compressed (or expanded) spectrum had to be multiplied.

The position L of the Compton edge (in channels) in the measured spectra corresponding to Compton electron energy E was calculated (Tabs. 1 & 3) with the following formula:

$$L = (E - E_o) * C * c_x \qquad (1)$$

A minimum least-square fit (non-weighted) routine from the SPEKT [Di-78] program was used for the task. Spectra were fitted over a region selected to exclude significant differences due to background at lower amplitudes. The quality of the fit can be seen on Figs. 2- 5 where the measured, the calculated (before folding) and the fitted spectra are presented for several resolution parameters together with markers indicating fitting ranges and a rough position of the Compton edge. Fitted spectra of single energy photon sources (Fig. 2) are in reasonable agreement with the measured, except for the very low energy region where the measured spectrum was always higher, probably due to scattering on all surrounding materials. The more complicated task was to fit a spectrum with two edges. Two methods were employed:

- the calculated spectra were combined with respect to the abundance of the γ-lines and then fitted to the measured one.

https://doi.org/10.7795/130.20231025

This method was employed in the case of the ^{60}Co (Fig. 3) source where the edges are scarcely distinguishable.

- the spectrum fitted to the edge corresponding to the greater energy is subtracted from the measured one before fitting the second edge. This method was used for ^{22}Na and ^{88}Y sources (Fig 4).

As the code does not take into account pair production and wall

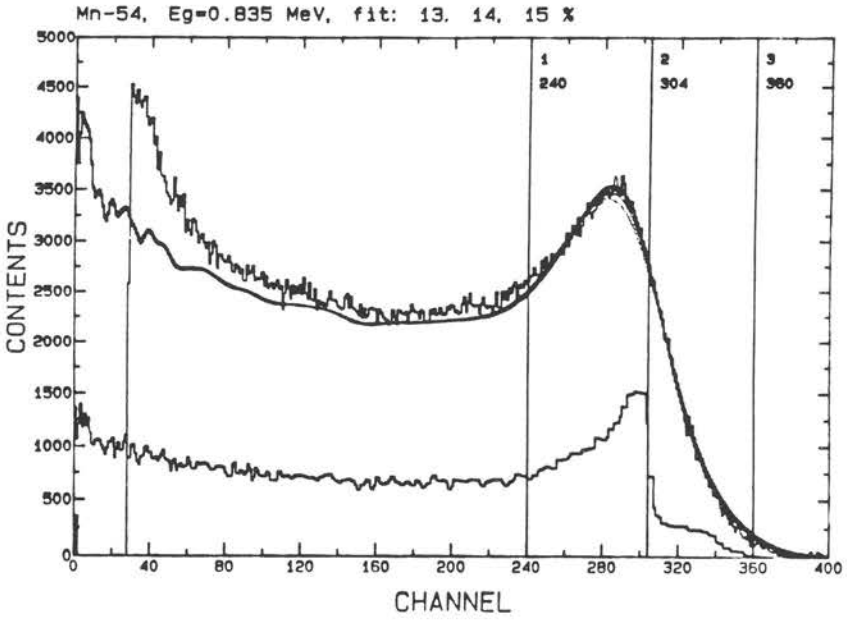

Fig. 2: Measured, calculated and fitted spectra for ^{54}Mn source. a marker depicts the fitting range and approximate position of the Compton edge.

effects at higher energies, the double-escape peak and the Compton edge of the 4.44 MeV photon cannot be adequately described (Fig. 5).

Three different sets of calibration measurements for both low and high gain were performed before, during and after the calibration measurements with neutrons. For the second set of LG calibration the resolution of the ADC was digitally expanded four times to enable lower-energy sources to be used. The results are

https://doi.org/10.7795/130.20231025

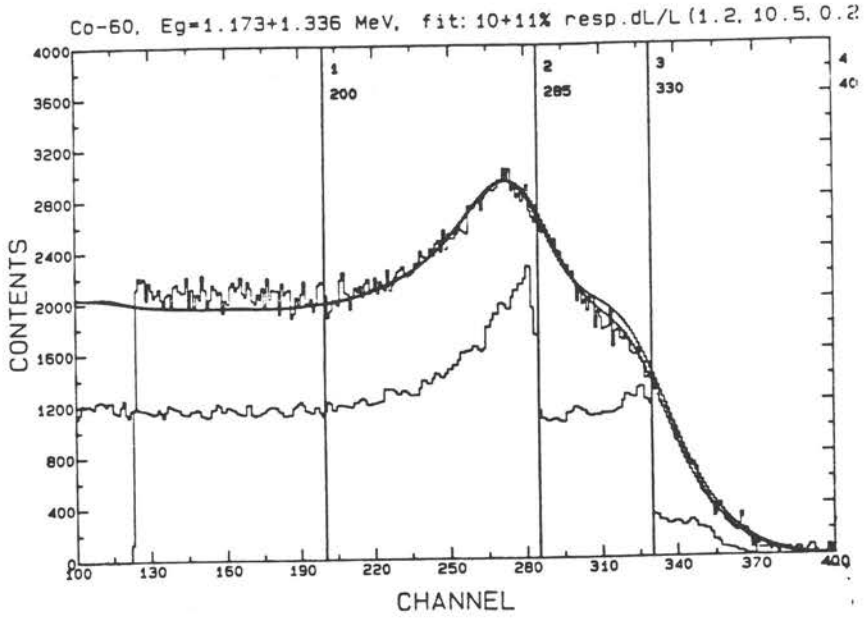

Fig. 3: Measured, calculated and fitted spectra for ^{60}Co source. Markers depict the fitting range and approximate positions of the Compton edge.

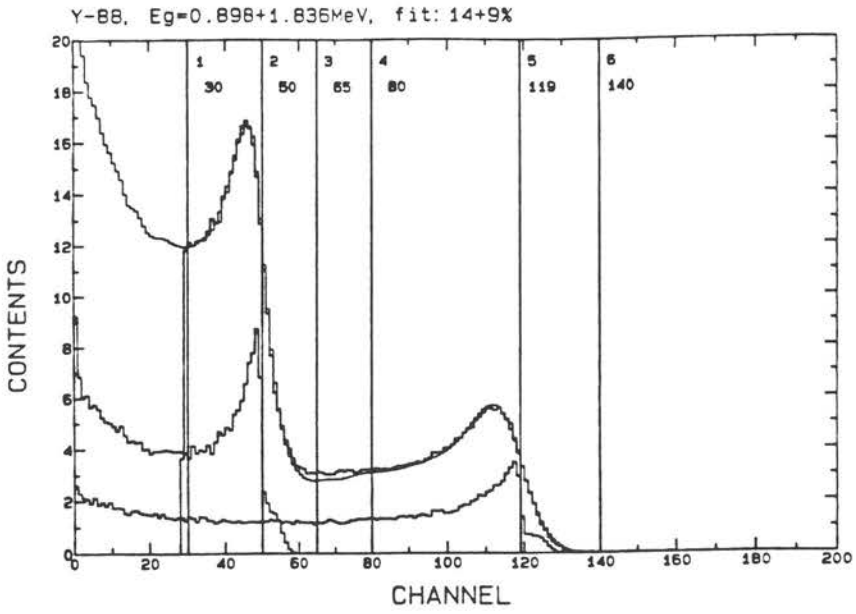

Fig. 4: Measured, calculated and fitted spectra for ^{88}Y source. Markers depict the fitting range and approximate positions of the Compton edge.

https://doi.org/10.7795/130.20231025

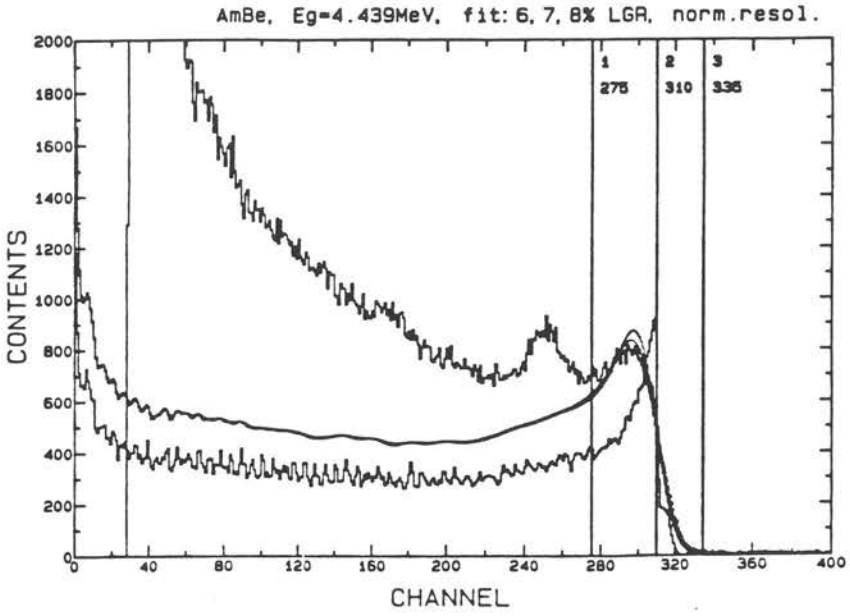

Fig.5: Photon spectrum measured with an AmBe neutron/photon source fitted at the upper edge with the response calculated for 4.44 MeV photons. Markers depict the fitting range and approximate position of the Compton edge.

summarized in Tabs. 1 & 2. A line

$$E = G * L + E_o \qquad (2)$$

was fitted using a non-weighted minimum least-square fit (code LIREG) to each set of E and L values to obtain the energy offset E_o and the slope G. Values of the light output corresponding to the fitted line L_c are also given in Tabs. 1 & 2. The parameters of the lines are in Tab.5.

https://doi.org/10.7795/130.20231025

Tab.1: Results of the γ calibraton for HGR; for explanation see text.

	E [keV]	L [chan.]	L_c [chan.]	$L - L_c$ [chan]	$(L-L_c)/L_c$ [%]	source	c_x
	341.	159.1	159.3	-0.2	-0.15	Na-22	0.9862
	477.	224.8	224.6	0.2	0.10	Cs-137	0.9924
	639.	301.1	302.3	-1.2	-0.38	Mn-54	0.9893
1	699.	333.7	331.0	2.7	0.80	Y-88	1.0020
	907.	430.7	430.8	-0.1	-0.02	Zn-65	0.9948
	1061.	502.5	504.7	-2.2	-0.43	Na-22	0.9914
	1612.	769.7	768.9	0.8	0.10	Y-88	0.9979
	341.	154.9	154.9	0.1	0.05	Na-22	0.9607
	477.	218.7	219.6	-0.9	-0.41	Cs-137	0.9655
	639.	296.0	296.8	-0.8	-0.27	Mn-54	0.9727
2	699.	329.8	325.4	4.4	1.36	Y-88	0.9900
	907.	424.2	424.4	-0.3	-0.06	Zn-65	0.9797
	1061.	493.9	497.8	-3.9	-0.78	Na-22	0.9744
	1612.	761.6	760.2	1.4	0.18	Y-88	0.9873
	341.	154.5	154.3	0.2	0.11	Na-22	0.9581
	639.	294.2	296.3	-2.1	-0.71	Mn-54	0.9667
3	699.	330.4	324.9	5.5	1.70	Y-88	0.9918
	1061.	491.5	497.3	-5.8	-1.17	Na-22	0.9697
	1612.	762.0	759.8	2.2	0.29	Y-88	0.9879

For each photon energy an average edge position (from the three sets) was calculated (Tabs. 3 & 4) and also fitted by a line.

https://doi.org/10.7795/130.20231025

Tab. 2: Results of the γ calibration for LGR.

	E [keV]	L [chan.]	L_c [chan.]	$L - L_c$ [chan]	$(L-L_c)/L_c$ [%]	source	c_x
1	699.	49.6	50.3	-0.7	-1.32	Y-88	0.9654
	907.	64.7	65.0	-0.3	-0.40	Zn-65	0.9694
	1061.	75.5	75.8	-0.3	-0.45	Na-22	0.9662
	1612.	116.7	114.8	1.9	1.69	Y-88	0.9815
	3417.	241.3	242.3	-1.0	-0.41	C-12esc	
	4197.	297.7	297.4	0.3	0.10	C-12	0.9596
2	477.	32.8	33.2	-0.4	-1.27	Cs-137	0.9395
	639.	44.5	44.8	-0.3	-0.65	Mn-54	0.9482
	699.	49.8	49.0	0.7	1.53	Y-88	0.9696
	907.	64.2	63.9	0.4	0.58	Zn-65	0.9622
	1061.	74.5	74.8	-0.3	-0.44	Na-22	0.9532
	1612.	114.0	114.1	-0.1	-0.07	Y-88	0.9585
3	699.	48.0	48.8	-0.8	-1.61	Y-88	0.9344
	1061.	74.6	74.3	0.2	0.31	Na-22	0.9543
	1612.	114.0	113.3	0.7	0.63	Y-88	0.9584
	3417.	241.0	240.8	0.2	0.10	C-12esc	
	4197.	295.5	295.9	-0.4	-0.13	C-12	0.9525

Tab.3: Averaged positions of Compton edges from three measurements for HGR. Max. diff. is the maximum difference of an edge position in a single measurement from the averaged position.

E [keV]	L [chan.]	L_c [chan.]	$L - L_c$ [chan]	$(L-L_c)/L_c$ [%]	source	max.diff [%]
341.	156.2	156.5	-0.4	-0.23	Na-22	2.
477.	221.8	221.5	0.3	0.14	Cs-137	1.4
639.	297.0	298.8	-1.7	-0.58	Mn-54	1.4
699.	331.3	327.4	3.9	1.19	Y-88	0.8
907.	427.4	426.7	0.8	0.18	Zn-65	0.7
1061.	496.0	500.2	-4.2	-0.84	Na-22	1.4
1612.	764.4	763.1	1.3	0.17	Y-88	0.7

https://doi.org/10.7795/130.20231025

Tab.4: Averaged positions of Compton edges from three measurements for LGR. Max. diff. is the maximum difference of an edge position in a single measurement from the averaged position.

E [keV]	L [chan.]	L_c [chan.]	$L - L_c$ [chan]	$(L-L_c)/L_c$ [%]	source	max.diff [%]
477.	32.8	33.5	-0.7	-2.03	Cs-137	0.
639.	44.5	45.0	-0.5	-1.05	Mn-54	0.
699.	49.1	49.2	-0.1	-0.16	Y-88	2.4
907.	64.5	63.9	0.5	0.86	Zn-65	0.5
1061.	74.8	74.8	0.0	0.06	Na-22	0.9
1612.	114.9	113.8	1.1	0.96	Y-88	0.9
3417.	241.1	241.5	-0.3	-0.14	C-12esc	0.1
4197.	296.6	296.7	-0.1	-0.03	C-12	0.1

Tab.5: Slope and offset calculated for measurement sets and averaged values for both gains; diff means difference of G values for meas. sets from the averaged value.

	high gain run			low gain run		
	E_o [keV]	G [keV/chan]	diff [%]	E_o [keV]	G [keV/chan]	diff [%]
1. set	8.784	2.085	-0.5	-12.471	14.155	+0.1
2. set	15.828	2.100	+0.2	10.303	14.043	-0.6
3. set	16.991	2.099	+0.2	8.650	14.156	+0.1
averaged	12.973	2.095	--	3.650	14.134	--

Discussion and conclusions:

▸ An almost random spread of positive and negative values of $(L-L_c)/L_c$ in Tabs. 1- 3 confirmed the linearity of $L_e(E)$. The values in Tab. 4 may be interpreted as an indication of nonlinearity but this is probably due to problems with a proper description of the response for 4.4 MeV photons already mentioned.

▸ The spectra used for the fits were calculated assuming that the offset E_o, which takes into account nonlinearity of the low energy part of $L_e(E)$, is 5 keV. The mean value for HGR and LGR $\mathbf{E_o}$ = **8.3 keV**. The uncertainty of this value was estimated to be 30 %[2].

---

[2] This value was obtained from a weighted least-square fit of a line through Compton edge positions L (using code AOP). The un-

https://doi.org/10.7795/130.20231025

The assumed value is then inside a one-sigma interval around the evaluated value and it can be taken as a confirmation of the supposed value.

▸ The calibration constant connecting light output in [redacted] l.u. with that in the ADC channels is given by the slope G defined by eq.(2). For HGR the slope calculated from averaged values G^{HGR}= $2.095*10^{-3}$ l.u./channel[3] was taken for the following measurements. In the case of LGR, the value G^{LG}= $14.043*10^{-3}$ l.u./channel calculated for the second measurement set instead of that for averaged positions was chosen. The reason for this is that the second measurement set was performed with the best statistics, and with extended resolution and all pure γ sources were used. A comparison between responses for neutrons for HGR and LGR later proved this choice to be the right one. The most important value for the combination of measurements with different gains is the ratio of its slopes $R^{L/G}$= G^{LG}/G^{HG}= 6.703.

▸ The differences between the slope G corresponding to averaged values and that one corresponding to single measurement sets (the last column of Tab. 5) can be taken as the reproducibility of the calibration. Values from +0.1 % to -0.6 % correspond to the estimated uncertainty of the G value for a single measurement set. This was estimated to be 0.4 % taking into account an estimated uncertainty of 0.5 % for each edge position L. Another influence which causes a spread of values greater than expected for both gain runs is that due to the necessity to readjust the high voltage when changing between LGR and HGR.

▸ The last result of the γ calibration procedure is the estimate of the resolution function dL/L (where dL=FWHM) used for

---

certainty of L's was estimated to be 0.5%. The offset was determined less precisely than the slope but it is no importance for the scale defined by the calibration.

[3] We use l.u. (previously defined) because this unit of light output is employed later to avoid confusing neutron and electron energies.

https://doi.org/10.7795/130.20231025

the folding of simulated responses. The values are presented in Tab. 6. and plotted in Fig.14 together with the corresponding values deduced from the response for monoenergetic neutrons. The scatter of dL/L values from the three measurements for each energy is about ± 5 %.

Tab. 6: Resolution of the detector (width of folding Gaussian) as function of the energy.

source	E [keV]	dL/L [%]
Na-22	341	19.5
Cs-137	477	14.5
Mn-54	639	13.
Y-88	699	13.
Zn-65	907	11.
Na-22	1061	10.5
Y-88	1612	8.5
C-12	4197	6.5

https://doi.org/10.7795/130.20231025

4. Calculation of neutron energies.

The experiment consisted of seven runs with different projectile energies. In each run (except that for 16 MeV neutrons) spectra listed in Appendix 3 were recorded with both low and high gains of the detector chain. The deuteron energies were so chosen that the corresponding energies of the zero-degree neutrons from the $D(d,n)^3He$ reaction were between 10 and 16 MeV in steps of 1 MeV. Neutron TOF spectra are shown in Fig. 6 for $E_d \cong$ 7 and 8 MeV. In addition to the peak corresponding to monoenergetic neutrons from the $D(d,n)^3He$ reaction, a broad continuum of neutrons ("break-up region"), from the D(d,np) reaction can be seen.The spectra are contaminated by small peaks below the monoenergetic peak from reactions on carbon and oxygen in the target entrance foil and the backing. Separate gas - out runs were performed with the reference detector only. The TOF spectra due to "satellites" (the position of the corresponding satellite peak is indicated by "S" in Fig. 6) have the same structure but are shifted in time [Ca-90].

For each run six windows were set in the TOF neutron spectrum (Figs. 6): one which covered neutrons from the D(d,n) reaction and five in the break-up part of the spectrum. The width of a TOF window was set to correspond to about ½ of the expected FWHM of the pulse height spectrum as estimated from the γ calibration and a guess light output function [Ve-68]. A comparison of these TOF window widths and the evaluated FWHMs is shown in Tab. 8. The positions of these TOF windows were selected to cover a neutron energy range of 1 - 10 MeV in 0.25 MeV steps and to avoid including the satellites. The data acquisition system recorded the pulse-height (PH) spectrum (the response) corresponding to each TOF window. In this way we obtained the detector response for six neutron energies in each run.

Deuteron and the neutron energies (see Tab. 7) were determined by means of the SPEKT program (using Nnn.SPE routines; nn=energy). The TOF spectra of neutrons+γ (K6-see App.3) and neutrons

https://doi.org/10.7795/130.20231025

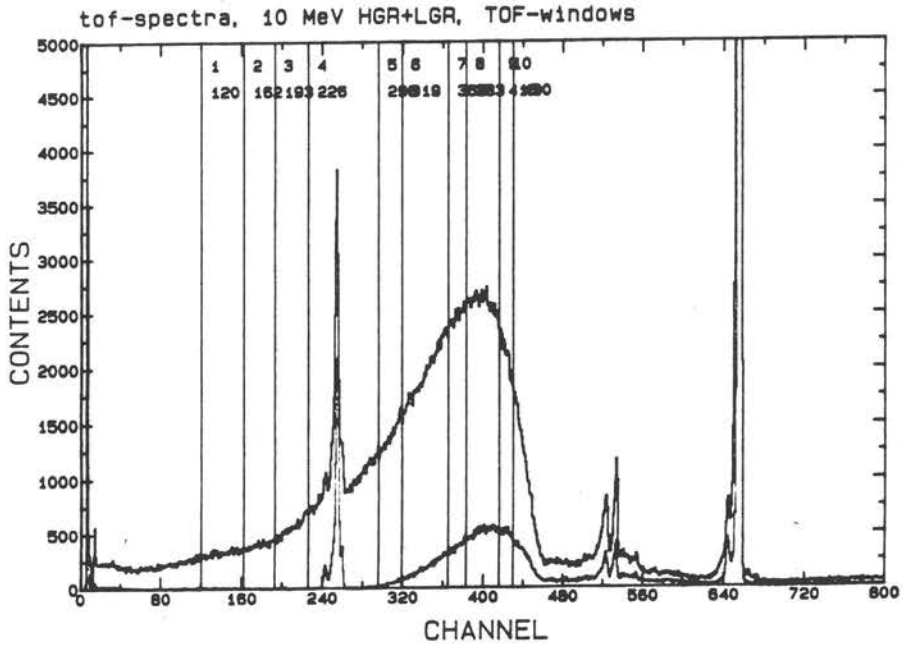

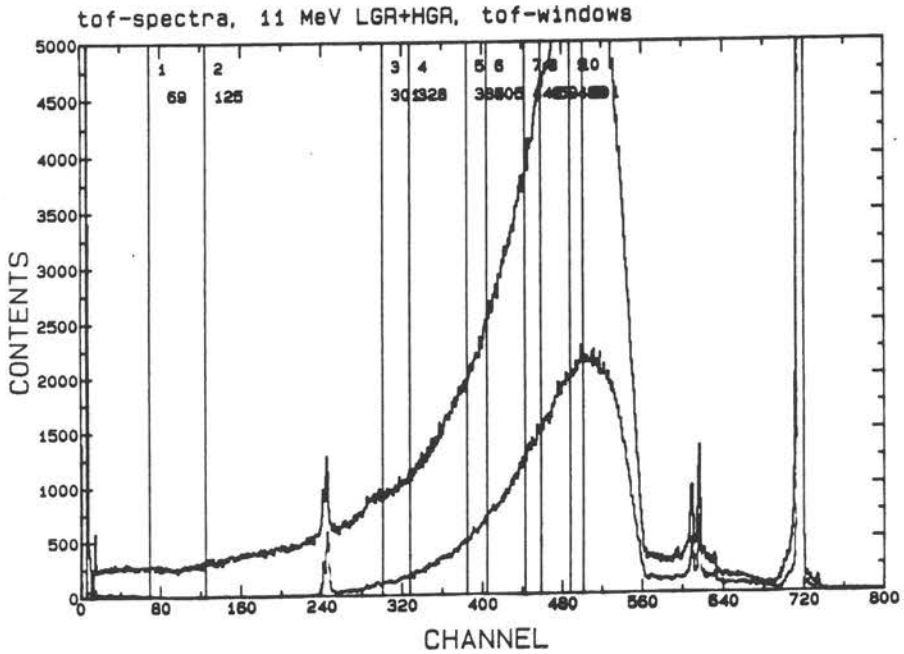

Fig. 6: TOF spectra for HGR (higher curve) and LGR for 10 and 11 MeV neutron energy runs. Vertical lines mark TOF windows for selection of monoenergetic neutrons.

https://doi.org/10.7795/130.20231025

alone (K8) were first corrected for channel overflows at the monoenergetic neutron and prompt γ peaks, and then the centre of gravity and the variance of these peaks were determined. The position of the γ-peak was corrected for the exact position in the target assembly where most of the photons are produced[4]. The energies of deuteron projectiles and the neutrons from the $D(d,n)^3He$ reaction were calculated from the distance between neutron and γ peaks, flight path (12 m) and time calibration constant[5]. The width of the neutron peak was calculated from the spread of deuteron energies estimated for a 3 cm long gas target filled with deuterium (pressure about $0.2*10^6$Pa). The differences between the peak positions are less than 0.04 % for both gains; the neutron energies and the corresponding mean deuteron energies in the target differ by less than 0.3 % and 0.5 % respectively, (see Tab. 7).

Tab. 7: Parameters of seven runs.

γ-peak [chan.]		n-peak [chan.]		correct.time [ns]	cal. ns/ch.	neut. ener. [MeV]		deut. ener. [MeV]	
LGR	HGR	LGR	HGR			LGR	HGR	LGR	HGR
899.6	899.9	655.3	655.3	0.59	0.9680	9.999	9.977	6.777	6.754
949.7	949.5	717.0	716.8	0.35	0.9676	10.894	10.888	7.727	7.720
899.7	900.1	680.4	680.8	0.11	0.9680	12.055	12.049	8.967	8.960
899.9	900.5	691.4	691.6	0.13	0.9675	13.151	13.106	10.147	10.099
901.1	901.5	699.5	699.7	-0.29	0.9680	13.904	13.980	10.965	10.950
950.8	950.8	755.6	755.3	-0.47	0.9675	14.714	14.666	11.851	11.798
900.7		714.5		-0.43	0.9678	15.923		13.133	

---

[4] For deuteron energies approx. < 10.5 MeV most of the photons are created in the target Mo entrance foil, while at higher energies they are chiefly created in the Au backing of the gas target. In each case the position of the γ-peak is corrected for photon production at the center of the target. The correction described in [Bo-87] and included in the SPEKT code was used and is presented in Tab. 7.

[5] The time calibration constant was determined for the set-up of TAC and ADC in the TOF branch. It was determined for each run by means of a precision time generator.

https://doi.org/10.7795/130.20231025

The neutron TOF spectrum (K8 Fig. 6) was then deleted between the TOF windows and transformed into an energy spectrum using the corrected position of the γ peak. The almost trapezoidal peak shape corresponding to the TOF window in the break-up region was analyzed to find its mean and and Gaussian width (FWHM). These are shown with their differences for both LGR & HGR in Tab. 8. The energies calculated for LGR & HGR differ by less than 0.3 %, except in the case of 1., 1.25, 1.50 and 2. MeV where the energy calculated for HGR might be viewed cautiously due to time walk and jitter of the CFD in the TOF branch for very small amplitudes.

https://doi.org/10.7795/130.20231025

Tab.8: Evaluation of energies from monoenergetic and break-up regions; comparison of LGR and HGR.

mean energy [MeV]		dif [%]	FWHM [keV]		dif [%]	TOF window [chan.]	
LGR	HGR		LGR	HGR		from	to
1.250	1.260	0.8	88	91	3.7	120	161
1.502	1.510	0.5	100	94	-6.1	193	225
2.025	2.010	-0.7	93	101	8.6	296	318
2.515	2.508	-0.3	111	110	-1.2	365	382
3.007	3.002	-0.2	107	111	4.3	416	429
9.999	9.977	-0.2	125	125	-0.2	641	661
0.994	1.010	1.6	94	89	-5.3	69	124
1.768	1.765	-0.2	98	98	-0.5	301	327
2.276	2.276	0.0	105	105	0.0	385	404
2.772	2.774	0.1	113	113	0.8	443	458
3.280	3.282	0.1	119	118	-0.2	488	500
10.894	10.888	-0.1	112	112	-0.1	700	725
3.012	3.006	-0.2	112	111	-0.5	416	429
3.523	3.517	-0.2	122	122	-0.5	456	467
4.011	4.004	-0.2	122	123	1.1	487	496
4.532	4.522	-0.2	133	132	-0.6	514	522
5.030	5.018	-0.2	137	136	-0.2	536	543
12.055	12.049	0.0	104	104	0.0	667	687
3.266	3.256	-0.3	118	117	-1.1	437	449
3.781	3.770	-0.3	124	122	-1.8	473	483
4.297	4.284	-0.3	137	135	-1.6	502	511
4.780	4.767	-0.3	144	143	-0.9	525	533
5.535	5.518	-0.3	138	137	-0.7	555	561
13.151	13.106	-0.3	93	93	-0.3	678	698
3.516	3.510	-0.2	121	120	-0.8	457	468
4.503	4.496	-0.2	131	131	-0.5	514	522
5.496	5.487	-0.2	137	138	0.6	555	561
5.989	5.977	-0.2	158	157	-0.2	571	577
6.457	6.443	-0.2	150	149	-0.6	585	590
13.904	13.890	-0.1	91	91	-0.1	685	705
4.259	4.258	-0.0	134	135	0.7	551	560
5.250	5.248	-0.0	146	146	0.1	595	602
5.753	5.752	-0.0	147	147	0.1	613	619
6.480	6.478	-0.0	152	151	-0.3	635	640
7.531	7.530	-0.0	157	156	-0.3	661	665
14.714	14.666	-0.3	83	83	-0.4	742	762
5.037			120			537	543
6.010			158			571	577
6.990			170			598	603
8.023			173			621	625
9.011			203			639	643
15.923			78			700	725

https://doi.org/10.7795/130.20231025

5. Proton light output function determination.

From these irradiations we got PH spectra monoenergetic neutrons at 36 energies for both gains and for another 6 energies for LGR only in 0.25 MeV steps between 1 MeV and 6 MeV, in 0.5 MeV steps from 6 to 8 MeV and in 1 MeV steps from 8 to 16 MeV (some responses corresponded to almost the same energy for a consistency check). The responses were treated separately for both gains. Several responses were totally or partially out of the region of the ADC and so cannot be used for this purpose. Summing up, 58 responses were investigated in the following procedure (see Tab.9).

The light output function $L_p(E)$ for protons was determined by means of an iterative procedure. Similarly to the γ-calibration, the position of the edge corresponding to the energy of protons scattered with maximum energy transfer was estimated, by means of a theoretical response fitted to the measured one. The fitting procedure was again realized by means of the SPEKT code and special routines were employed for different tasks.

The iteration process started with a rectangular PH spectrum as the first approximation of a theoretical response assuming only one scattering of each neutron on a proton and neglecting all other reactions. The spectrum was folded by a Gaussian resolution function. Three parameters defining the shape of such a spectrum, height (amplitude), length (edge) $L_p^{ch}(E)$ and width of the folding Gaussian were gained from a least-squares fit to the measured spectrum performed by the F.SPE routine. An example is shown in Fig. 7. The position of the response edge $L_p^{ch}(E)$ (in channels) corresponding to the neutron energy E obtained from the fitted spectrum was converted to the scale in light units $L_p^{lu}(E)$ given by gamma calibration:

$$L_p^{lu}(E) = L_p^{ch}(E) * G \qquad (3)$$

where G is the slope of the light output scale determined by the γ-calibration.

The difference of the values $L_p^{lu}(E)$ from a reference

https://doi.org/10.7795/130.20231025

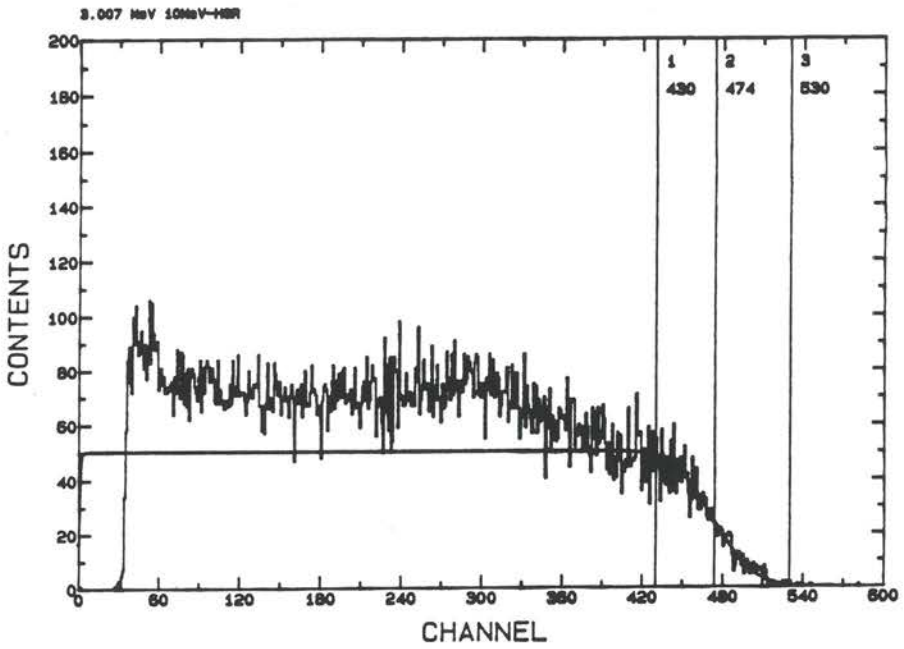

Fig.7: Fit of a rectangular spectrum to the 3.007 MeV response; horizontal lines idicate fit region and approximate position of the edge.

polynomial function for $L_p(E)$[6] (included in the NRESP7 code) was calculated by an auxiliary code DIFPOL and plotted[7] in Figs 8 & 9. A curve was drawn through the data points in Fig 9 in the range 0 - 8.5 MeV. The corresponding values were visually read in steps of 100 keV in the range from 0 - 3 MeV and in steps of 500 keV up to 8.5 MeV. This table of differences containing 42 points was inserted into the NLIGHT code (an auxiliary code used together with NRESP7) as a DATA statement. The code interpolates the table

---

[6] The reference polynomial function is given by:

$$L_p(E)=\begin{cases} 0.07269*E+0.11237*E^2 & 0 < E < 1.5 \text{ MeV} \\ -0.20570+0.35260*E+0.01343*E^2+0.00250*E^3, & 1.5 < E < 3.5 \text{ MeV} \\ -0.25999+0.34141*E+0.03303*E^2+0.00092*E^3, & 3.5 < E < 8.0 \text{ MeV} \\ -1.43180+0.69325*E, & 8.0 < E < 20. \text{ MeV} \end{cases}$$

[7] The difference from the standard polynomial function was used to enhance variations. It is clear from Fig. 9 that in contrast to Fig. 8, a statistical spread of values is not noticeable.

https://doi.org/10.7795/130.20231025

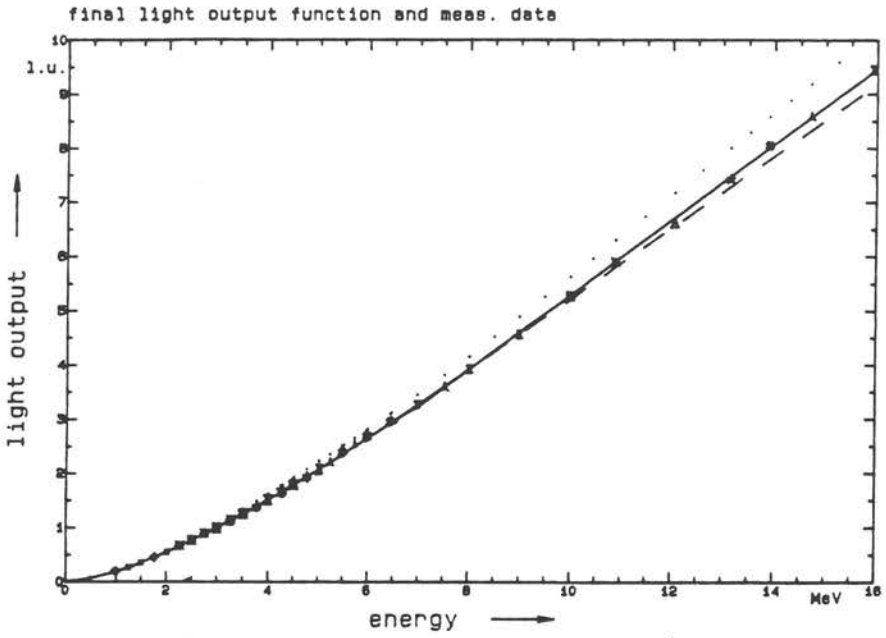

Fig.8: Three light output functions for protons;
—— determined function;
.....Verbinski's [Ve-68] light output function;
- - -function from table No. 10 from NRESP7.

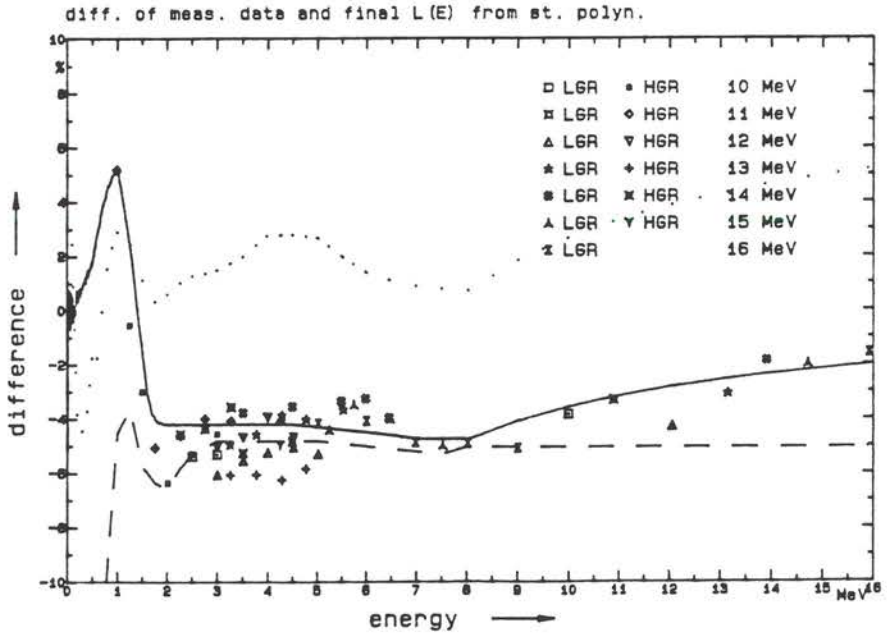

Fig. 9: Differences of three $L_p(E)$ from standard polynomial function; notation as in Fig.8.

https://doi.org/10.7795/130.20231025

yielding an output in the form of a table of $L_p(E)$ in 10 keV steps from 0 to 600 keV and then in 20 keV steps up to 8 MeV (a total of 431 points) .

For E > 8 MeV the $L_p(E)$ function is specified in the NRESP7 code by a linear function which is fitted (LIREG code) to the corresponding values of $L_p^{lu}(E)$. Two parameters of this function are inserted together with the table (of 431 points) into NWQ7C, a data file containing different light output functions used in the NRESP7 code to calculate the response in the next steps.

All 58 response functions were calculated by the NRESP7 code using energies and energy widths ($\Delta E/E$) for LGR determined as described above.

In the next and subsequent steps, the calculated response was first converted into the linear scale of light output with constant width C channels/l.u. (values 72 and 480 were now used for LGR and HGR respectively). As in the first step, the response was then folded by a Gaussian function and fitted to the measured

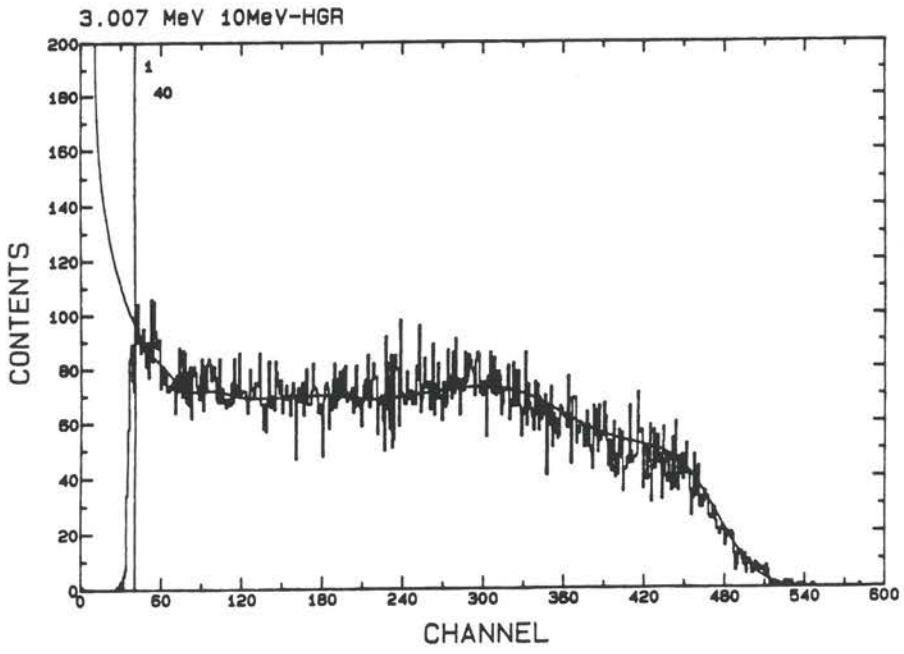

Fig.10: Calculated spectrum fitted to 3.007 MeV neutron response.

https://doi.org/10.7795/130.20231025

one (routine FIS.SPE). An example is shown in Fig. 10. Three parameters are finally extracted from the fit: the width dL/L of a Gaussian used for folding (relative FWHM of the detector), the compression factor c_x and the count rate factors by which the calculated spectrum had to be compressed or expanded and multiplied. The new light output table $L_{p,new}(E)$ was then calculated from the previous using the following equation:

$$L_{p,new}(E) = L_{p,old}(E) * C^g * c_x * G^g \quad , \; g = LGR, HGR \quad (4)$$

The results were again compared with the reference polynomial function $L_p(E)$, fitted and a new function $L_{p,new}(E)$ supplied the NRESP7 code in the proper representation. The process was iteratively repeated until the new $L_p(E)$ values confirmed the function used in the previous iteration. The scheme of the procedure is shown in Fig. 13.

Three iterations were necessary to determine the light output function for the IRD detector. The results are listed in Tab.9 and shown in Figs.8 & 9:

- Two runs substantially increased the spread of the values: the 13 MeV HG run and the 12 MeV LG run (see Fig. 8). From the comparison of all responses which were inside the ADC range for both gains[8] (Fig. 11) it can be seen that in both cases the detector gain was set about 1.5 - 2 % lower than during the γ-calibration or the mean of other runs.
- The scatter of measured values which indicates the uncertainty of $L_p(E)$ is less than ± 1 % except in the cases already mentioned.
- Two other examples of $L_p(E)$ are shown in Figs 8 & 9: the

---

[8] For 16 energy points between 2.5 and 4.25 MeV the response for both gains is completely in the ADC range. The responses for HGR were compressed by a factor 6.7031 (ratio of gains acquired in γ calibration) and then fitted to the corresponding LGR response. The compression factor is a measure of the consistency with the γ-calibration and is shown in Fig. 11.

https://doi.org/10.7795/130.20231025

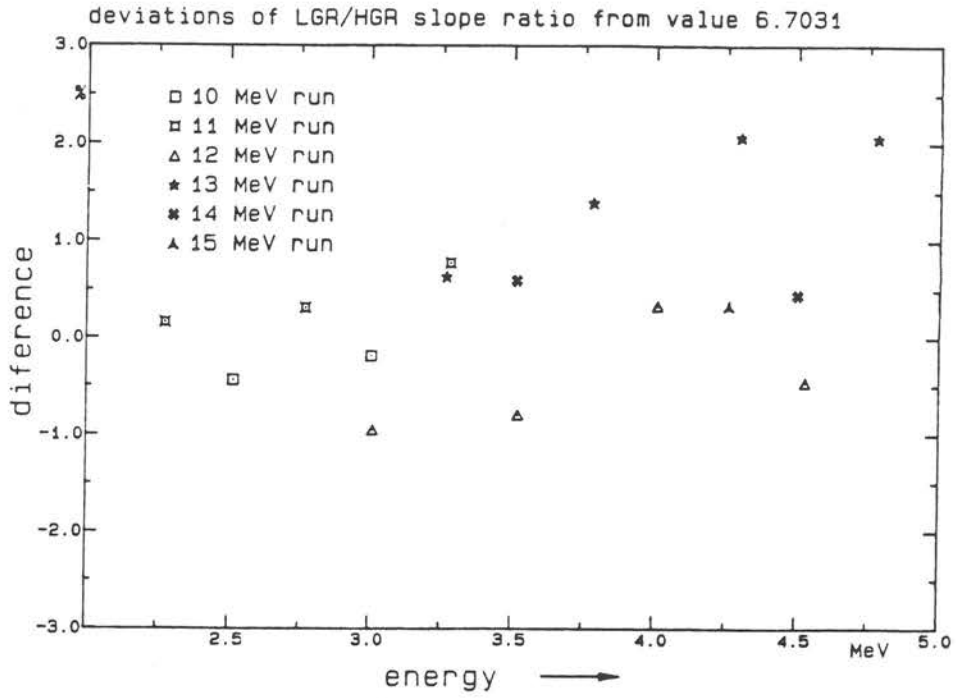

Fig. 11: Deviations of ratios of LGR/HGR slopes from the value 6.7031 determined by γ calibrations for responses where both L&HGR were in the ADC range.

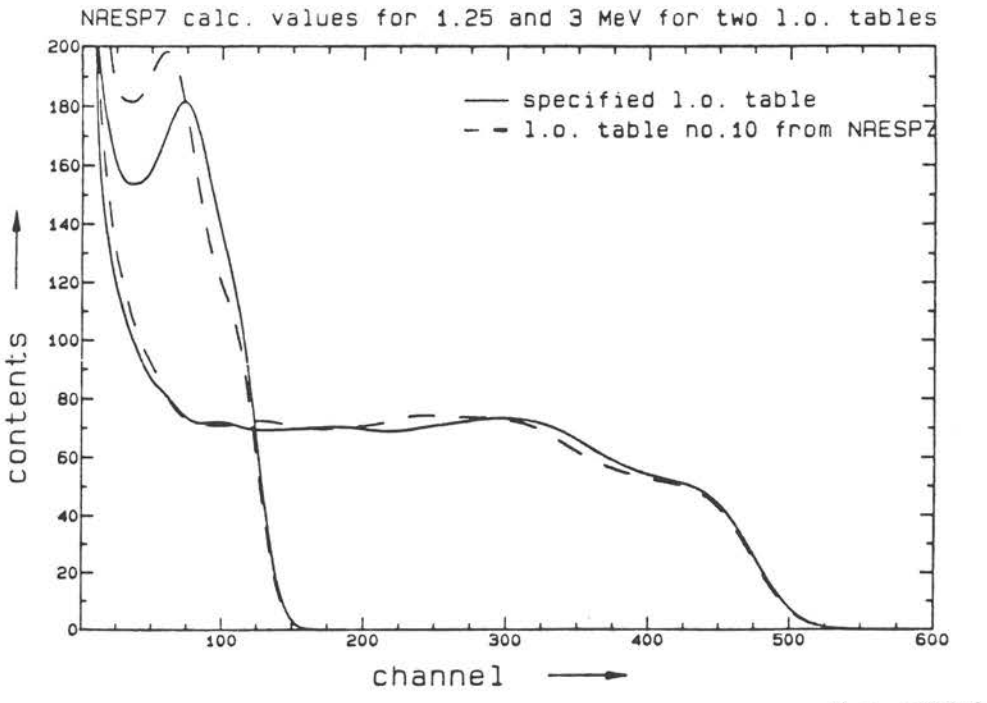

Fig. 12. Calculated responses for 1.25&3 MeV neutrons for two different "wrong" $L_p(E)$ mentioned in Figs. 8&9.

https://doi.org/10.7795/130.20231025

function published by Verbinski [Ve-68] which has been used for this detector until now and the function determined earlier in the PTB for a 1.5"*1.5" detector. This function has a similar shape in the 3 - 8 MeV region but its behavior is opposite between 0 and 2 MeV. A response function was calculated using this $L_p(E)$ for 1.25 & 3 MeV and fitted in the range of the edge to the measured one. Both are shown in Fig. 12. The lower

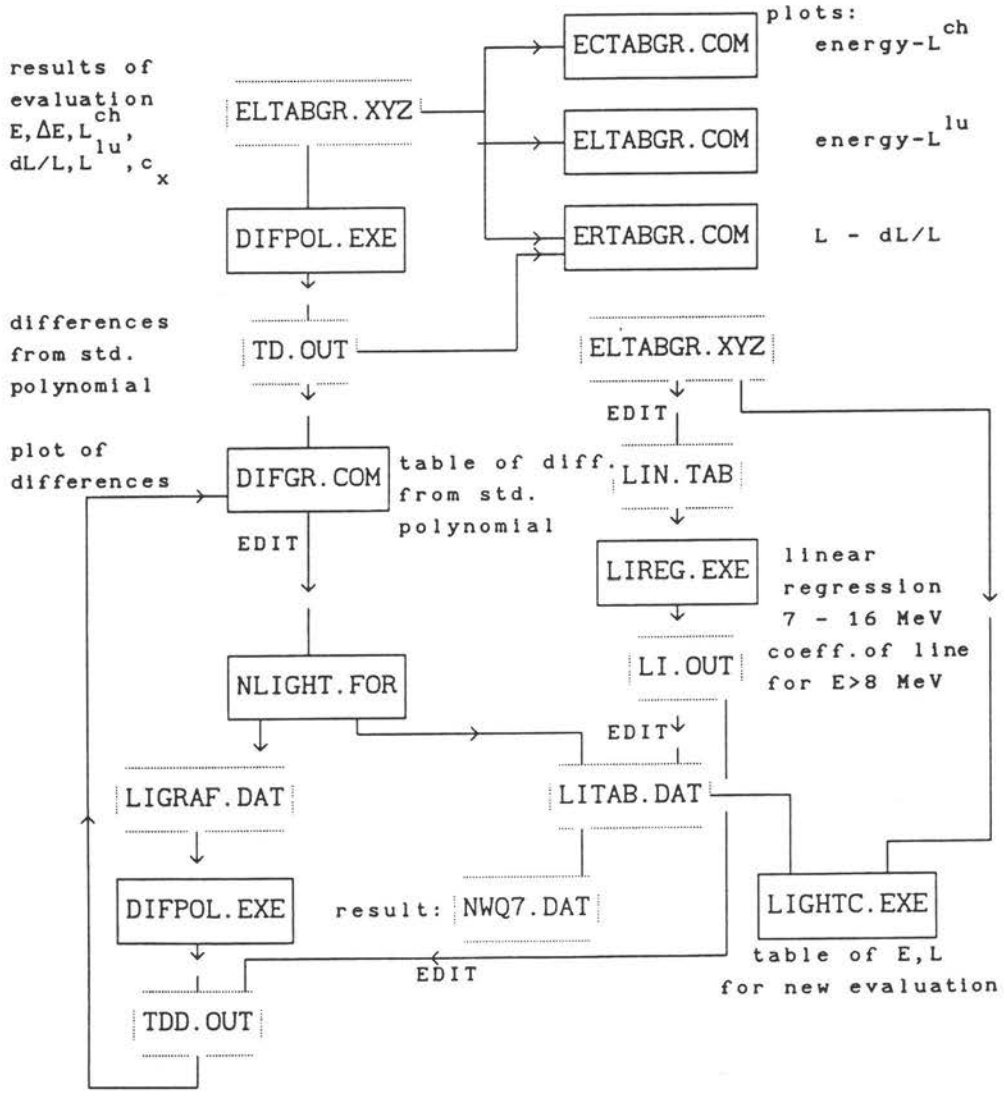

Fig.13: Scheme of evaluation of light output function; solid lines indicates software and doted lines data files.

values for $L_p(E)$ result in a shift of the second scatter

https://doi.org/10.7795/130.20231025

edge[9] (at channel 80 and 310). An increase in the range of lower amplitudes for the 1.25 MeV response will be discussed later.

- The maximum difference of 1 % of corresponding values for LGR and HGR in Fig. 9 confirmed the choice of the value for the slope of LGR taken from γ calibration. For the value G=14.134 corresponding to averaged values (Tab. 5) the maximum difference was almost twice.

During the determination of the light output function the resolution function of the IRD detector.was also determined. Values of the relative FWHM (dL/L) of the Gaussian used for folding are listed in Tab. 9 and in Fig.14 They are shown together with values measured for photons and a function

$$\frac{dL}{L}(E)=\sqrt{A^2+\frac{B^2}{L}+\frac{C^2}{L^2}} \qquad (5)$$

introduced in [Di-2-82]. Values for A=1.2, B=10. and C=0.2 were obtained from the figure. Later a fit of function (5) to all experimental values was performed with results A=1.5, B=10. C=3.46. This corresponds to a dashed curve in Fig. 14. The increase of parameter C which causes a better fit for very low amplitudes where experimental values have a rather large uncertainty, is unusually high. The values mentioned first are therefore used in the rest of this work.

---

[9] Due to nonlinearity the summed light output from two recoil protons (due to two fold neutron scattering) is lower then the maximum light output even if the full neutron energy is transferred.

https://doi.org/10.7795/130.20231025

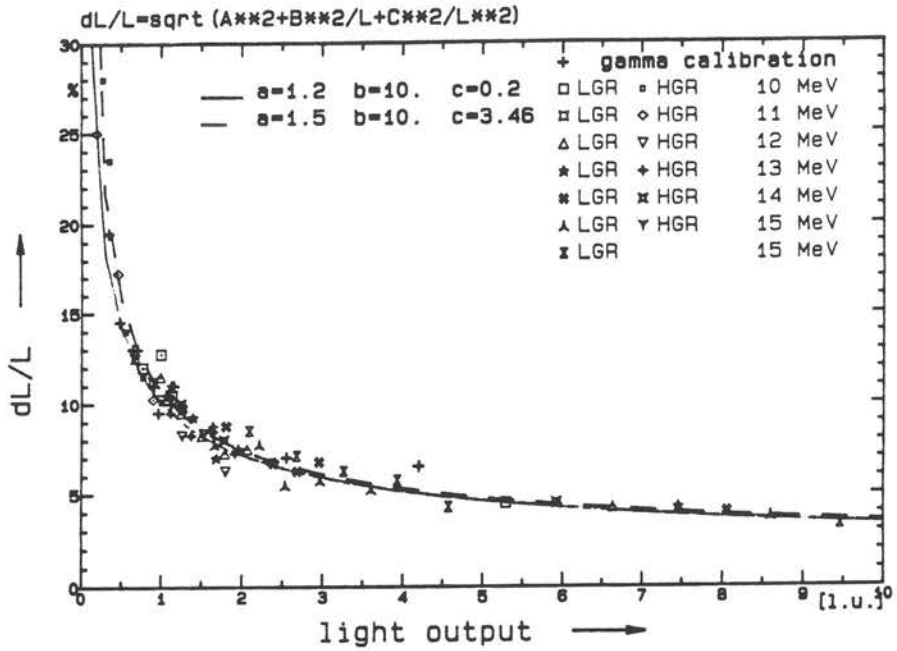

Fig.14: Resolution function obtained from measured values for both neutrons and photons.

https://doi.org/10.7795/130.20231025

Tab.9: Results of light output determination.

neut. energy E [MeV]	L_p^{ch} [channel]		L_p^{lu} [l.u.]		$\frac{\Delta E}{E}$ [%]	dL/L [%]		c_x [1]	
	LGR	HGR	LGR	HGR		LGR	HGR	LGR	HGR
1.260		124.9		0.2650	7.26		28.0		0.9813
1.510		166.3		0.3518	6.20		23.5		0.9917
2.025		259.5		0.5470	5.00		14.0		0.9797
2.515	54.1	362.8	0.7625	0.7633	4.39	12.0	11.5	0.9889	0.9833
3.007	70.2	474.1	0.9886	0.9965	3.71	12.75	10.1	0.9952	0.9835
9.999	376.4		5.2889		1.24	4.5		0.9872	
1.010		90.5		0.1928	8.85		25.0		1.0144
1.768		213.0		0.4495	5.53		17.25		0.9921
2.276	47.1	315.2	0.6641	0.6637	4.61	12.5	12.75	0.9949	0.9961
2.772	63.0	423.8	0.8877	0.8911	4.06	11.25	10.25	0.9947	1.0012
3.280	81.1	540.4	1.1415	1.1353	3.62	10.5	10.25	1.0015	0.9994
10.894	421.2		5.9186		1.03	4.5		0.9891	
3.012	69.8	472.8	0.9833	0.9939	3.71	11.5	10.25	0.9722	0.9900
3.523	88.1	595.6	1.2399	1.2511	3.47	9.5	8.25	0.9770	0.9928
4.011	106.5	714.1	1.4988	1.5193	3.03	8.25	8.35	0.9799	0.9868
4.532	126.9	853.9	1.7852	1.7922	2.93	7.25	6.25	0.9816	0.9919
5.030	146.5		2.0608		2.72	7.5		0.9799	
12.055	471.8		6.6297		0.86	4.25		0.9746	
3.266	79.4	525.8	1.1181	1.1049	3.59	11.0	9.5	0.9809	0.9785
3.781	98.5	650.0	1.3870	1.3654	3.23	9.25	8.25	0.9849	0.9777
4.297	119.2	778.9	1.6766	1.6351	3.16	7.0	8.75	0.9922	0.9754
4.780	138.3	909.1	1.9449	1.9079	3.01	7.5	7.25	0.9913	0.9799
5.535	170.3		2.3947		2.50	6.75		0.9966	
13.151	530.3		7.4505		0.71	4.25		0.9837	
3.516	89.5	590.3	1.2595	1.2400	3.42	9.75	10.0	0.9932	0.9865
4.503	127.7	844.8	1.7971	1.7732	2.92	8.75	8.0	0.9955	0.9900
5.496	169.2		2.3789		2.50	6.7		0.9997	
5.989	190.7		2.6818		2.63	6.25		1.0018	
6.457	210.0		2.9521		2.33	6.75		0.9954	
13.904	573.4		8.0550		0.66	4.0		0.9932	
4.259	117.5	779.7	1.6540	1.6368	3.15	7.75	8.25	0.9929	0.9807
5.250	157.0		2.2078		2.78	7.75		0.9894	
5.753	180.0		2.5312		2.56	5.5		1.0001	
6.480	211.0		2.9658		2.34	5.75		0.9961	
7.531	256.3		3.6029		2.08	5.25		0.9873	
14.714	612.0		8.5972		0.57	3.75		0.9919	
5.027	148.1		2.0836		2.39	8.5		0.9909	
6.010	190.0		2.6718		2.62	7.1		0.9938	
6.990	231.9		3.2595		2.43	6.25		0.9883	
8.023	279.3		3.9249		2.16	5.75		0.9872	
9.011	325.2		4.5703		2.25	4.3		0.9789	
15.923	673.1		9.4559		0.49	3.3		0.9936	

https://doi.org/10.7795/130.20231025

6. Light output function for α particles.

$L_\alpha(E)$ is represented in the NRESP7 code by a combination of exponential and linear functions. Parameters of these functions were corrected in each step parallel to the correction of the light output function for protons in order to minimize differences between peak positions due to $C(n,\alpha)$[10] reactions in calculated and measured responses. The results of the final correction when the multiplication parameters were decreased by 11% in comparison with the reference function from NRESP7 (used there for about five detectors of different sizes) are shown Fig 15. The final function used for the IRD detector is:

$$L_\alpha(E) = \begin{cases} 0.021 * E^{1.871} & \text{for } E < 6.76 \text{ MeV} \\ 0.65314 + 0.20755 * E & \text{for } E \geq 6.76 \text{ MeV} \end{cases}$$

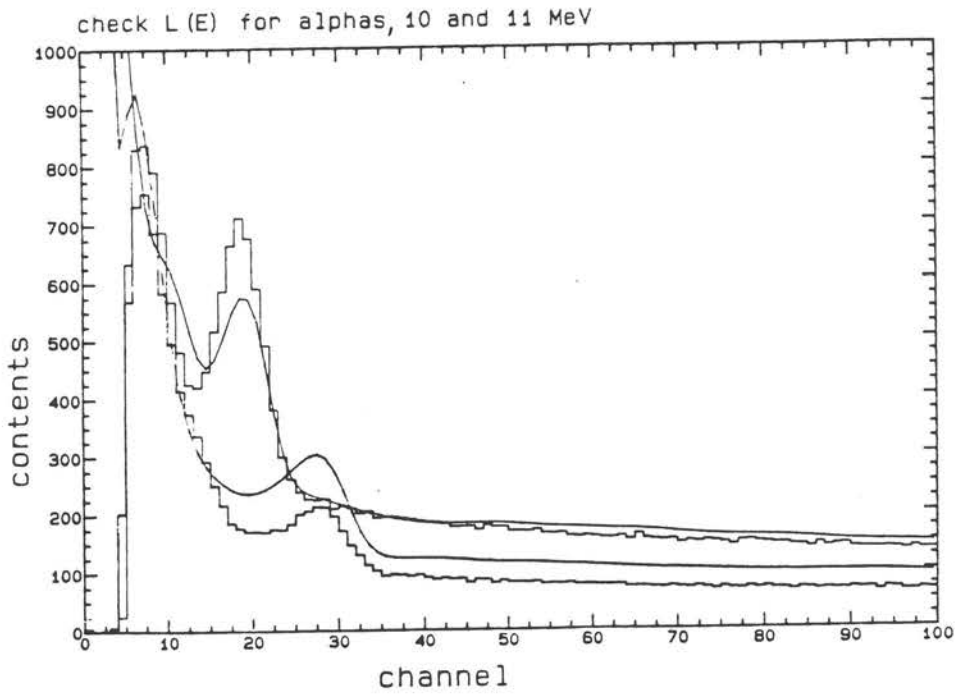

Fig. 15: Measured and calculated responses for 10 and 11 MeV neutrons. Spectra are arbitrarily scaled in the y-axis.

---

[10] The maximum energy of α particles corresponding to the energy of 12 MeV neutrons is about 10 MeV.

https://doi.org/10.7795/130.20231025

7. Normalization to the reference detector.

7.1. Normalization.

The normalization is performed relative to the measurements with a calibrated reference detector [Bo-88]. The response for each energy (TOF window) of each run was multiplied by the ratio

$$F^{M} = \frac{M^{ref}}{M^{det}} * \frac{1}{R^{div}} \qquad (6)$$

where M^{ref} is the monitor count for the reference detector run;
M^{det} is the monitor count for the studied detector run;
R^{div} is the ratio by which the incoming count rate was divided to avoid overloading the data acquisition system.

7.2. Dead-time correction.

The normalization must be completed by dead time corrections. Due to the monitor normalization, only the detector counts had to be corrected. Monitor counts were not corrected as the monitor counts were taken in the same way in the measurement with both detectors and, so, the dead time corrections cancel out.
Two approaches to the dead time corrections were used:

- The different dead-time of the detector electronics and data acquisition system must be combined; this approach is valid for PTB-based systems, where the PH, PS and TOF signals are valid only when they have passed a three-fold coincidence.
- Besides the dead times mentioned in the previous case, there is a dead-time of the TOF branch which should be combined with the dead time of the analog part. This can be used for the IRD system, where the TOF branch is partially independent.

Three dead-time corrections which were combined according to the approach:

Data acquisition dead time correction:
The cumulated dead-time of data acquisition system (DAS - digital

https://doi.org/10.7795/130.20231025

part starting with ADCs) T^{DAS} is recorded by the system analyzer and the correction is

$$f^1 = \frac{T^{DAS}}{T^m} \qquad (7)$$

where T^m is the measuring time of the run.

Detection chain dead time correction.

When all three branches of the detector chain are joined by a coincidence the detector electronics system has one dead time. In the case of the IRD detection system, two separate dead times for PH & PS and TOF branches were measured. The dead time can be taken as a gap between the zero point and the continuous part at the spectrum (Fig. 16) of the time intervals between two subsequent pulses of EVENT output signals of the G&D generator and the TAC output signals in the TOF branch .

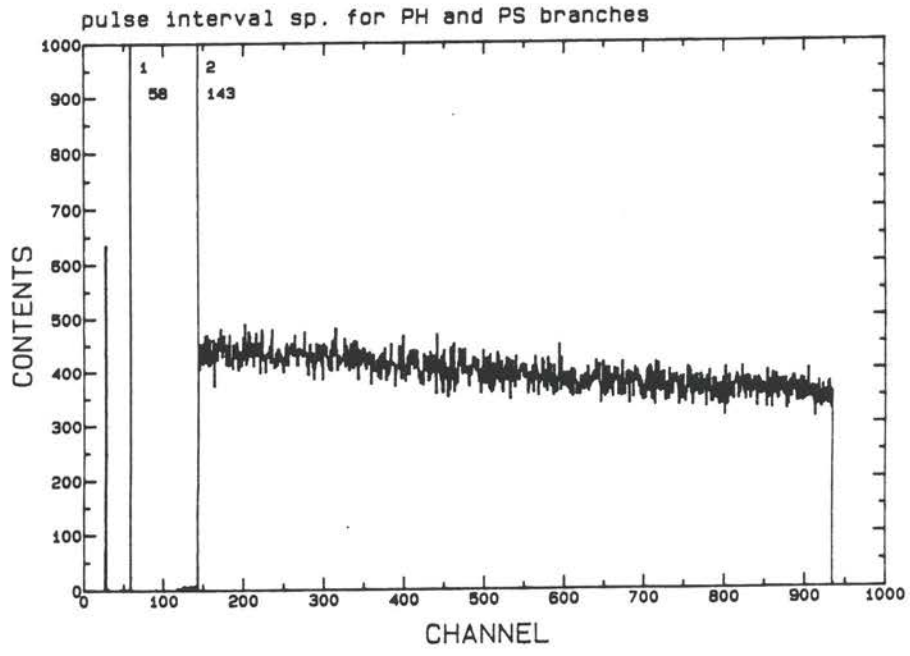

Fig 16: Spectrum of time intervals between subsequent pulses for PH & PS branches.

This dead time was τ^{EVENT}= 6 μs for the PH & PS branches and

https://doi.org/10.7795/130.20231025

τ^{TOF}=9.14 μs for the TOF branch. The correction for the detection chain is then

$$f^2 = \max (n^{EVENT} * \tau^{PH\&PS}, n^{CF} * \tau^{TOF}) \qquad (8)$$

where n^{EVENT} or n^{CF} are the EVENT or the CF count rate in the run (during measurements count rates and the dead-time of the TOF branch were both higher - see Tab.10).

Correction for dead-time for separate TOF branch.

Due to the long timing constants of the CFD-TAC in the TOF branch the processing of a previous event in the TOF branch may not be finished when the PH and PS branches have already processed the next event. In that case PH analysis may be performed but the ADC of the TOF branch converts only a steady current level which appears in the TOF spectrum as a small peak from 3 to 13 channels. The ratio of this peak area to the integral of the TOF spectrum r^{TOF} creates the basis for the dead time correction:

$$f^3 = r^{TOF} \qquad (9)$$

When eqs. (N-1)-(N-4) are combined **the final normalization factor** is

$$F^{NORM} = F^M * (1+f^t) \qquad (10)$$

where f^t is the total correction.

For the **first version of the dead-time correction** using the independent TOF branch approach, f^t amounts to:

$f^t = f^3 + f^1$ for $R^{div} = 1/1$

$= f^3 + n^{EVENT} * \tau^{PH\&PS}$ for $R^{div} < 1/1$

The dead time of the separate TOF branch should always be counted. To this is added dead-time of the DAS or the PH&PS branch.

The **second version of the dead-time correction** uses

$f^t = f^1$ for $R^{div} = 1/1$

$= f^2$ for $R^{div} < 1/1$.

For R^{div}=1/1 i.e. no pulses were rejected, in which case DAS dead-time dominates and only the f^1 correction is used. For R^{div} lower

https://doi.org/10.7795/130.20231025

than 1/1 (values from 1/2 to 1/4 were taken) the probability that two events will occur in the DAS within 20 μs (estimated time for conversion and data collection cycle) is negligible. In this case the dead-time of detection chain plays a more important role.

All values mentioned in this part and measured for the IRD detector are listed in Tab. 10: f^E and f^C are two values from which f^2 is selected and the lower subscript of f^t refers to the first or second version of the dead time corrections.

Tab.10: Normalization coefficients and dead-time corrections. Quantities are explained in the text; run 10H means 10 MeV HGR run.

Run	M^{det}	M^{ref}	R^{di}	F^M	f^1	f^E	f^C	f^3	f^t_1	F^{NORM}_1	f^t_2	F^{NORM}_2
	counts	counts			%	%	%	%	%		%	
10L	57312	113652	1/1	1.983	0.81	0.19	0.61	0.46	1.27	2.008	0.81	1.999
10H	114459	113652	1/1	0.993	1.17	0.28	0.79	1.72	2.89	1.022	1.17	1.005
11L	57742	115350	1/1	1.998	0.98	0.25	0.65	0.58	1.56	2.029	0.98	2.017
11H	114753	115350	1/1	1.005	1.64	0.32	0.82	1.97	3.81	1.042	1.64	1.022
12L	98940	100560	1/2	2.033	0.67	0.30	0.99	1.07	1.37	2.061	0.99	2.053
12H	98403	100560	1/2	2.044	1.02	0.50	1.22	2.46	2.96	2.105	1.22	2.069
13L	47309	94922	1/2	4.013	0.90	0.42	1.11	0.59	1.01	4.054	1.11	4.057
13H	95032	94922	1/2	1.998	1.23	0.60	1.42	2.71	3.31	2.064	1.42	2.026
14L	86837	90214	1/2	2.078	1.13	0.50	1.72	0.51	1.01	2.099	1.72	2.114
14H	44205	90214	1/4	8.163	0.97	0.88	2.17	0.89	1.77	8.308	2.17	8.340
15L	37396	50735	1/2	2.713	0.92	0.42	1.18	0.86	1.28	2.748	1.18	2.745
15H	37492	50735	1/2	2.706	1.44	0.62	1.52	1.66	2.28	2.768	1.52	2.747
16L	21022	20793	1/3	2.967	1.04	0.69	2.70	3.31	4.01	3.072	2.70	3.047

Ratios of PH spectra integrals over the overlapping part of LGR and HGR were calculated (see the next paragraph) for both detection chain dead-time corrections. The second version underestimates LGR less and the same correction as for PTB-based detectors was then also selected for the IRD detector in spite of the fact that the separate TOF branch concept seemed to be more feasible for the IRD detector. The F^{NORM}_2 was used for the later evaluation.

https://doi.org/10.7795/130.20231025

8. Comparison and combination of low and high gain measurements.

All measurements and most of their evaluations were performed separately for L&H gains but before unfolding, PH spectra for LGR & HGR should be compared and combined. An agreement of PH spectra integrals for both gains over overlapping regions can also be used as a check of the n-γ discrimination.

For the set-up used, the lower limit of the overlapping interval is, given by the threshold of LGR. It was approx. 0.525 l.u. (channel 38) for the 10, 12, 14 and 16 MeV runs and approx. 0.3 l.u. (channel 22) for the remaining runs. The upper limit is given by the range of the ADC for HGR and it is approx. 2.1 l.u. (channel 150). To compare PH spectra integrals, corresponding responses for LGR & HGR were multiplied by the corresponding coefficients F^{NORM} and the HGR response was compressed to the LGR scale (by the factor 6.7031 as determined in the γ calibration).

For each pair of responses (LGR & HGR) a subinterval of the overlapping region was selected to avoid influencing the spectrum

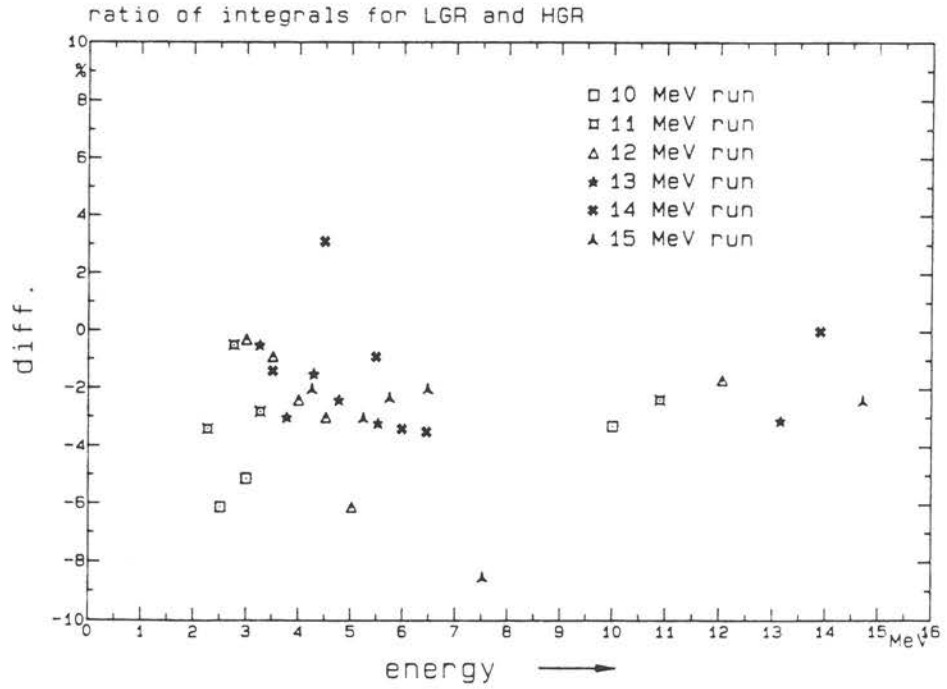

Fig. 17: Ratio of PH spectra integrals over LGR and HGR overlapping regions.

https://doi.org/10.7795/130.20231025

end, and the ratio of integral was calculated. The results are given in Tab. 11 and in Fig. 17.

With the exception of five values, all data are in the strip 2 % wide around line -2 %. It is clear that some neutrons (1÷5 %) are missing in the LGR response and that this amount slightly in

Tab.11: Differences between integrals of responses in the interval shown for LGR and HGR (after compression). The responses for energies lower than 2 MeV were not compared due to the very short range.

Energy	Integ. over range		L/H int. diff.
MeV	l.u.		%
2.515	0.562	0.702	-6.1
3.007	0.562	0.843	-5.1
9.999	0.843	1.685	-3.3
2.276	0.421	0.562	-3.4
2.772	0.421	0.702	-0.5
3.280	0.562	0.843	-2.8
10.894	0.562	1.685	-2.4
3.012	0.562	0.702	-0.3
3.523	0.562	0.843	-0.9
4.011	0.632	1.053	-2.4
4.532	0.843	1.685	-3.0
5.030	0.843	1.685	-6.1
12.055	0.843	1.685	-1.7
3.266	0.421	0.843	-0.5
3.781	0.562	0.843	-3.0
4.297	0.562	1.194	-1.5
4.780	0.562	1.403	-2.4
5.535	0.562	1.685	-3.2
13.151	0.562	1.685	-3.1
3.516	0.843	1.053	-1.4
4.503	0.843	1.264	+3.1
5.496	0.843	1.685	-0.9
5.989	↓	↓	-3.4
6.457			-3.5
13.904			0.
4.259	0.843	1.403	-2.0
5.250	↓	1.685	-3.0
5.753		↓	-2.3
6.480			-2.0
7.531			-8.5
14.714			-2.4

https://doi.org/10.7795/130.20231025

creases for energies below 3 MeV. This might be explained by some errors in the n-γ discrimination.

To estimate a possible influence of the interval selection, a ratio of integrals depending on the lower limit was calculated. A constant upper limit was selected at channel 140 (10 channels above ADC upper limit) and at channels 30 and 40 for lower limits (sufficiently above the threshold). Ratios $r_i^{L/H}$ were calculated according to the following formula:

$$r_i^{L/H} = \frac{\sum_{k=i}^{140} h_k^L}{\sum_{k=i}^{140} h_k^H} \qquad i=40(30),\ldots,140 \qquad (11)$$

where h_k^L and h_k^H are normalized responses for LGR and HGR. Spectrum $r_i^{L/H}$ for the 15 MeV run is shown in Fig. 18 as an example. Values

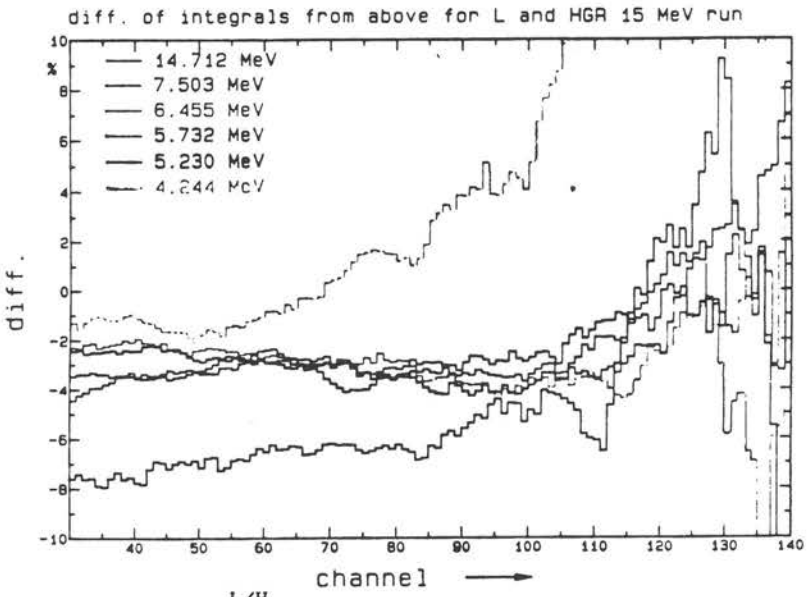

Fig. 18: Spectra $r_i^{L/H}$ (see text) for 15 MeV run.

for 4.25 MeV (highest curve) and for 7.5 MeV (lowest curve) are far from a stable ratio for the lower limit between channels 60 and 110. The 4.25 MeV ratio for the upper limit higher than 60 is apparently influenced by the near response edge (channel 117) but the second case is extraordinary and can hardly be explained.

https://doi.org/10.7795/130.20231025

9. Calculation of fluence.

The neutron fluence at the position of the detector was determined by a comparison of measured and calculated responses. The response is calculated by NRESP7 for fluence $1/cm^2*MeV$ at the detector center. The FIR.SPE routine was used to find a multiplication factor to fit the calculated to the measured responses: The calculated response was compressed by the factor c_x from the final fit during determination of the $L_p(E)$ function (an optimum fit of calculated and measured responses) and then an integral spectrum was calculated (integral of the response from above). The corresponding integral spectrum was also calculated for the measured response. The ratio $r_i^{E/C}$

$$r_i^{E/C} = \frac{\sum_{k=i}^{1023} h_k^E}{\sum_{k=i}^{1023} h_k^C} \qquad (12)$$

(where h_k^E and h_k^C are experimental and calculated responses respectively) of these spectra is a constant when full agreement between experiment and calculation was achieved in shape, and this constant (multiplied by F^{NORM}) is the fluence Φ. In most cases $r_i^{E/C}$ spectra have a plateau between the threshold and the second scatter edge.

Channel I was chosen as a lower end of the plateau:

I=40 for 10, 12 and 14 MeV LG runs,

I=25 for 11, 13 and 15 MeV LG runs,

I=40 for HGR,

for all responses to neutrons with energies below 10 MeV. For higher energies the limit I was increased to channel 90 because of an increasing disagreement due to the influence of reactions on carbon[11]. The fluence is then given by:

---

[11] The influence of reactions on carbon already starts at approx. 7.5 MeV but responses to neutrons between 7 and 9 MeV were measur-

https://doi.org/10.7795/130.20231025

$$\Phi = F^{NORM} * r_I^{E/C} \qquad (13)$$

Fluences calculated separately for LGR & HGR are given together with values of the limit I in l.u.in Tab. 12. As in the comparison of overlapping regions fluences calculated for HG runs are about 2 % higher. A clear tendency is also apparent in the table and Fig. 19: with decreasing energy the LGR/HGR discrepancy increases. As in the previous case the reason is probably an imperfect n-γ discrimination.

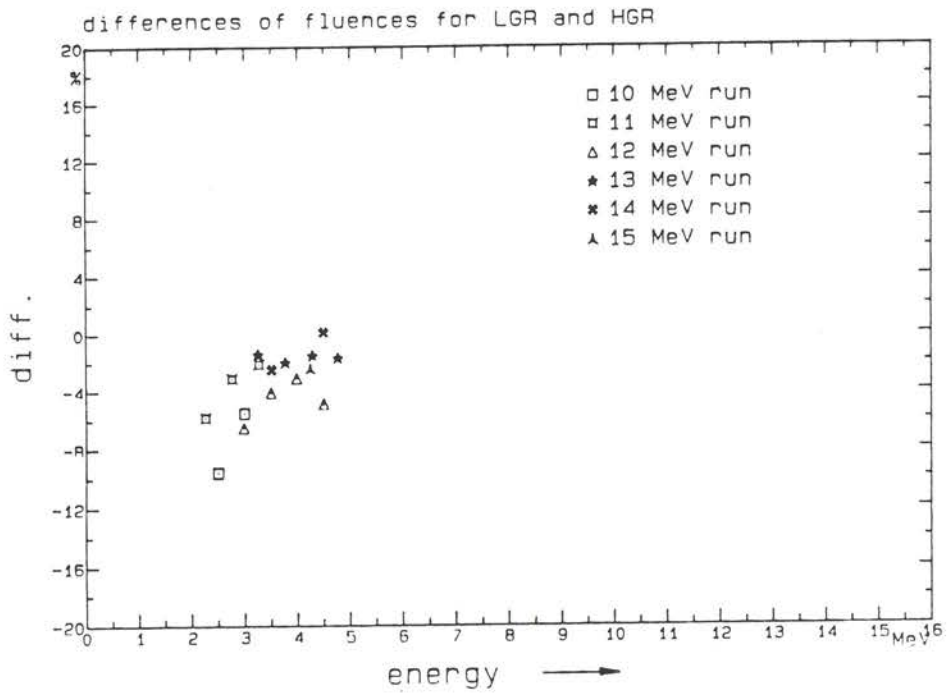

Fig.19:Differences between fluence values calculated for LGR & HGR.

The reliability of the fluence estimate with respect to the choice of limit I is apparent from Figs. 20 & 21. where for two examples (11 MeV run and responses to (d,n) neutrons) the normalized ratio $\tilde{r}_i^{E/C}$

---

ed during the 16 MeV run when only LGR with a higher threshold was used.

https://doi.org/10.7795/130.20231025

$$\tilde{r}_i^{E/C} = \frac{r_i^{E/C}}{r_I^{E/C}} \qquad i=1,\ldots,1023 \qquad (14)$$

are presented. From these figures and values of $\tilde{r}_i^{E/C}$ for other responses it can be concluded that if the integration limit I is set between the values used and the values corresponding to the second scatter edge, the fluences will be in the range of ± 4 % according to the values in Tab. 12.

In the section devoted to $L_p(E)$ determination the case of wrongly selected $L_p(E)$ was discussed. When using this light output function, the fluence was about 6.5 % and 2.2 % higher for 1.25 MeV and 3 MeV responses respectively.

A "reference" detector (REF) whose previous results were compared with those from neutron telescope [Bo-88, Si-85] was irradiated simultaneously with the IRD detector. The differences between the fluences evaluated by the two detectors are given in Tab. 12 and in Fig. 22. We see a systematic shift very slightly

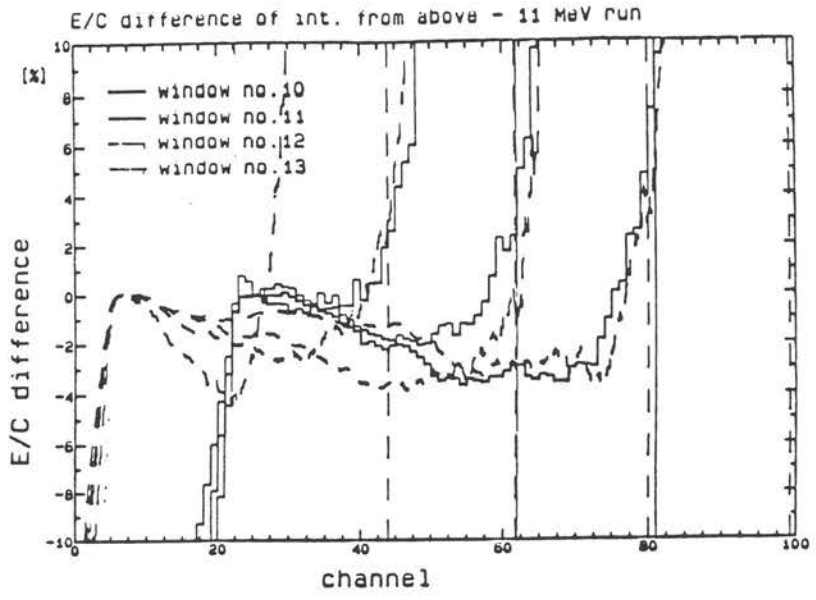

Fig. 20: Spectra of normalized ratios $\tilde{r}_i^{E/C}$ for 11 MeV for LG & HG runs. Windows refer to TOF windows coresponding to different energy responses.

https://doi.org/10.7795/130.20231025

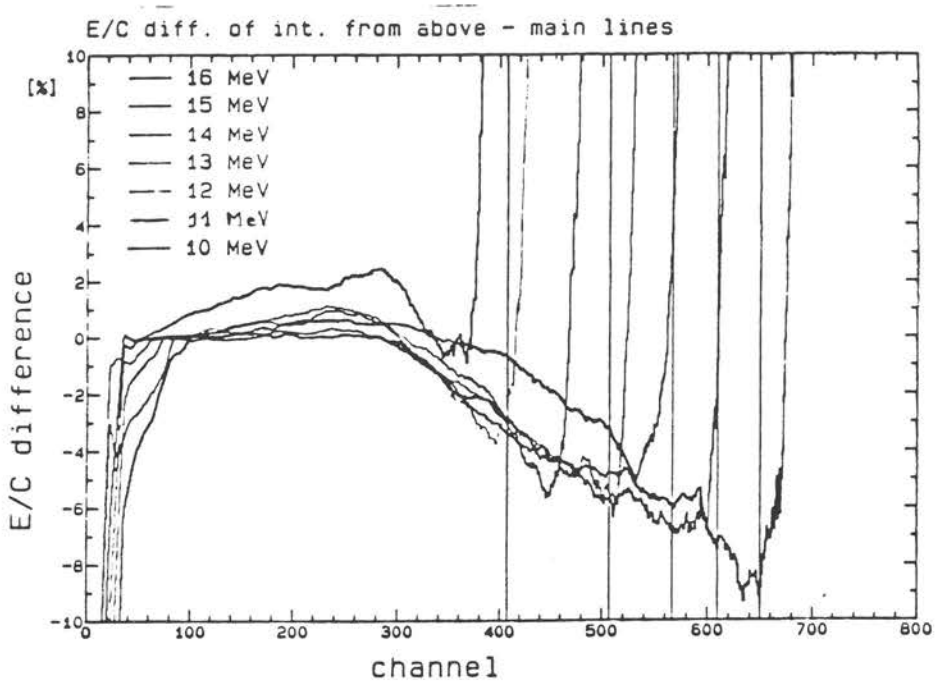

Fig. 21: Spectra of normalized ratios $\tilde{r}_i^{E/C}$ for responses to neutrons with energies greater than 10 MeV.

dependent on energy: - 2÷4 % for the lowest energies and - 1÷3 % for the highest. In 16 cases between 2.25 and 4.25 MeV we have data from both LGR and HGR. The LGR data are always lower and this seemed to confirm the hypothesis about relatively higher-set PS discrimination for LGR. When HGR data are taken where available and LGR anywhere else, we will get an almost energy independent fluence correction factor of between 2 and 4%.

https://doi.org/10.7795/130.20231025

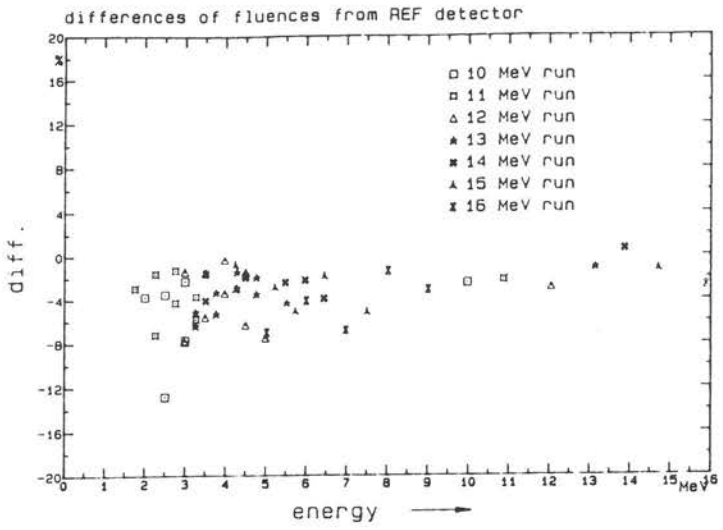

Fig. 22: Differences between fluences of IRD detector and REF detector.

https://doi.org/10.7795/130.20231025

Tab. 12: Fluences measured for LGR and HGR, their relative diff. and differences from "reference" (REF) detector.

Energy MeV	limit of integ l.u.* 10^{+3}		Fluence $10^{-3} * cm^{-2}$		L/H diff. [%]	diff. from REF [%]	
	LGR	HGR	LGR	HGR		LGR	HGR
1.261	↑	↑		1.671			
1.510	↑	↑		2.186			
2.009	561.7	↑		3.861			-3.7
2.508	↓	↑	5.025	5.558	-9.6	-12.8	-3.5
3.002	↓	↑	3.683	3.897	-5.5	-7.7	-2.3
9.977	561.7	↑	172.204			-2.5	
1.007	↑	↑		1.839			
1.761	↑	↑		3.199			-2.9
2.270	351.1	↑	5.134	5.448	-5.8	-7.2	-1.6
2.766	↓	↑	8.532	8.805	-3.1	-4.3	-1.3
3.272	↓	↑	10.065	10.285	-2.1	-5.8	-3.7
10.873	561.7	↑	191.250			-2.2	
2.993	↑	↑	7.700	8.233	-6.5	-7.8	-1.4
3.502	↑	↑	11.754	12.258	-4.1	-5.6	-1.5
3.986	561.7	↑	14.029	14.484	-3.1	-3.4	-0.3
4.502	↓	↑	14.103	14.835	-4.9	-6.3	-1.4
4.997	↓	↑	8.663			-7.5	
12.050	842.6	↑	188.139			-2.9	
3.257	↑	↑	8.626	8.748	-1.4	-6.4	-5.1
3.770	↑	↑	12.371	12.629	-2.0	-5.3	-3.3
4.285	351.1	83.8	17.784	18.060	-1.5	-2.9	-1.4
4.768	↓	↓	22.304	22.688	-1.7	-3.5	-1.9
5.522	↓	↓	18.368			-4.3	
13.144	1053.3	↓	201.772			-1.1	
3.509	↑	↓	9.556	9.800	-2.5	-4.1	-1.6
4.495	↑	↓	17.794	17.773	0.1	-1.8	-1.9
5.488	561.7	↓	23.435			-2.4	
5.979	↓	↓	24.526			-2.2	
6.446	↓	↓	17.874			-3.9	
13.870	1122.9	↓	205.136			0.6	
4.244	↑	↓	8.555	8.762	-2.4	-3.0	-0.7
5.230	↑	↓	14.411			-2.8	
5.732	351.1	↓	15.830			-5.0	
6.455	↓	↓	16.272			-1.8	
7.503	↓	↓	8.377			-5.1	
14.712	1263.9	↓	123.347			-1.2	
5.023		↓	8.489			-7.0	
6.006	491.5	↓	14.553			-4.1	
6.986	↓	↓	17.182			-6.8	
8.022	↓	↓	14.351			-1.4	
9.012	561.7	↓	5.405			-3.1	
15.892	1263.9	↓	106.082			-2.8	

https://doi.org/10.7795/130.20231025

10. Generation of response matrix

Setting up $L_p(E)$ enabled the detector response matrix which consists of detector responses to neutrons with different energies, to be calculated. The usefulness of a response matrix for unfolding is shown by the grid of the neutron energies for which responses are calculated (or measured) and by the light output grid (l.o.) in which responses are presented. Both grids were selected to acquire enough data for the generation of response matrices with reasonable dimensions that could be used for unfolding in the full range (1-20 MeV) or with a very high resolution in a limited energy region.

The energy range between 0.5 and 20 MeV was divided into 183 non-equidistant groups, so that the group width $(E_{j+1}-E_j)$ is approximately equal to $\frac{1}{4}$ of FWHM(E_j)[12]. Each response was calculated by means of the NRESP7 code for neutrons with a rectangular energy distribution between E_j and E_{j+1}. The NRESP7 code provides output PH spectra in two forms:

- PH spectrum in non-equidistant bin structure (800 bins) with edges

$$L_i = \left(\frac{i-1}{215.}\right)^2, \qquad i=1,\ldots,801 \qquad (15)$$

  where L_i is the light output in light units. The detector resolution is not taken into account in this spectrum.
- PH spectrum rebinned to an equidistant scale and then folded by a Gaussian function with the width proportional to FWHM(L).

The first form makes possible later rebinning and folding into different structures according to an actual unfolding task. This form was used to set-up the response matrix for the whole scale

---

[12] Edges of energy intervals were generated by the following empirical algorithm:

$$E_{j+1} = E_j\left(1 + \frac{0.02}{\sqrt{E_j}} + \frac{0.05}{E_j}\right) \quad \text{for } E_j = 0.5 \text{ MeV and } j=1,\ldots,183$$

https://doi.org/10.7795/130.20231025

unfolding. To include a detector resolution, the following folding procedure was developed.

The detector response is smeared (folded) for several reasons. The contribution of a certain bin to another is usually described by a Gaussian function. Then the contents of the i-th bin of the measured PH spectrum z_i (ranging from L_i to L_{i+1}) is expressed by the following equation:

$$z_i = \int_{L_i}^{L_{i+1}} dL' \int_{-\infty}^{+\infty} \frac{1}{\sqrt{2\pi}\,\sigma(L)} e^{-\frac{(L-L')^2}{2\sigma^2(L)}} f(L)\,dL, \quad i=1,\ldots N \qquad (16)$$

where f(L) is the non-folded PH spectrum. In spite of the fact that the non-folded PH spectrum f(L) has positive values only in the measured range $0 < L_1 < L_{M+1}$, the number of the folded spectrum bins N is theoretically infinite. But we will get non-negligible z_i only in the measuring range increased for "tails" on both ends of a response. The real length of the "tail" is about two detector FWHM's. When the lowest end of the non-folded spectrum is $L_1=0$, then the "tail" at negative light outputs has no sense and the folded spectrum starts at L_1. Then $N = M + M_{tail}$ where M_{tail} is approximately $2*FWHM(L_{M+1})$ in channels. The non-folded PH spectrum is a constant inside the j-th bin: $f(L) = f_j$ for $L \in <L_j, L_{j+1})$, $j=1,\ldots,M$. The second integral in (16) can then be divided to a sum M of integrals over light output bins. Assuming that

$$e^{-\frac{(L-L')^2}{2\sigma^2(L)}} = e^{-\frac{(L-\bar{L}_i)^2}{2\sigma^2(L)}} \quad \text{for } L' \in <L_i, L_{i+1}),\ i=1,\ldots N \qquad (17)$$

where $\bar{L}_i$ is the middle of i-th bin, we get

$$z_i = (L_{i+1}-L_i)\sum_{j=1}^{M} f_j \int_{L_j}^{L_{j+1}} \frac{1}{\sqrt{2\pi}\,\sigma(L)} e^{-\frac{(L-\bar{L}_i)^2}{2\sigma^2(L)}} f(L)dL, \quad i=1,\ldots N \qquad (18)$$

Assuming that the Gaussian width is approximated by a step

https://doi.org/10.7795/130.20231025

function i.e. $\sigma(L)=\sigma(\bar{L}_j)=\sigma_j$ for $L \in \langle L_j L_{j+1} \rangle$, we can define a folding matrix $\mathbb{G}$ as:

$$\mathbb{G}_{i,j} = \frac{1}{\sqrt{2\pi}\ \sigma_j} \int_{L_j}^{L_{j+1}} e^{-\frac{(L-\bar{L}_i)^2}{2\sigma_j^2}} dL, \quad \begin{matrix} i=1,\ldots,N \\ j=1,\ldots,M \end{matrix} \qquad (19)$$

Inserting (18) into (17) we then get

$$\hat{\mathbb{F}}_i = z_i/(L_{i+1}-L_i) = \sum_{j=1}^{M} \mathbb{G}_{i,j}\mathbb{F}_j \quad \text{i.e.} \quad \hat{\mathbb{F}} = \mathbb{G} * \mathbb{F}, \qquad (20)$$

for the folded spectrum $\hat{\mathbb{F}}$ where $\mathbb{F}$ is the vector of non-folded spectrum with M elements f_j. The elements of the folding matrix $\mathbb{G}$ can be calculated using the error function

$$\mathrm{erf}(x) = \frac{2}{\sqrt{\pi}} \int_0^x e^{-t^2} dt \qquad (21)$$

$$\mathbb{G}_{i,j} = \frac{1}{2}\left[\mathrm{erf}\left(\frac{L_{j+1}-\bar{L}_i}{\sqrt{2}\ \sigma_i}\right) - \mathrm{erf}\left(\frac{L_j-\bar{L}_i}{\sqrt{2}\ \sigma_i}\right)\right] \qquad (22)$$

To keep the normalization of a spectrum the following condition must be fulfilled:

$$\sum_i^N \hat{\mathbb{F}}_i = \sum_i^N \sum_j^M \hat{\mathbb{G}}_{ij}\mathbb{F}_j = \sum_j^M \mathbb{F}_j \sum_i^N \mathbb{G}_{ij} = \sum_j^M \mathbb{F}_j \Rightarrow \sum_i^N \mathbb{G}_{ij} = 1 \text{ for } j=1, \ ,M \qquad (23)$$

This condition is not generally fulfilled because of the limitation to positive values in (18) and rounding errors during the calculation of $G_{i,j}$ (erf is usually approximated in calculation). Non-negligible differences from unity are mainly for $\sum_i \mathbb{G}_{ij}$ with the lowest and highest j. This is corrected using $G^*_{i,j}$ instead of $G_{i,j}$, where

$$G^*_{i,j} = G_{i,j} \text{ for } i \neq j \text{ and } G^*_{i,i} = G_{i,i} + \left(1 - \sum_i \mathbb{G}_{ij}\right) \qquad (24)$$

The code MB (Matrix Builder) was written to set-up a response matrix for an actual application. First responses inside the ener-

https://doi.org/10.7795/130.20231025

gy range of interest are condensed to light output bins, the number of which can be used as an unfolding code. To avoid correlations, k bins are condensed to one where the integer k is selected on input. The condensed response is then folded according to the procedure described above. The Gaussian σ_j is calculated from the function dL/L (FWHM) determined by eq. (5):

$$\sigma_i = 2\sqrt{2\ \ln 2}\ \left(\frac{dL}{L}\right)_{\bar{L}_i} \qquad (25)$$

M_{tail} is set, in the code, to M-j where j<M is the lowest subscript for which $G_{M+M-j,j}$ > "limit of precision" (0.0001 used). A description of the MB input and output is given in Appendix 2.

https://doi.org/10.7795/130.20231025

11. Conversion of TOF to energy spectra.

The TOF spectra have already been used for the determination of the neutron energies corresponding to the TOF windows. Now they will be used for conversion to neutron energy spectra, normalized by the energy dependent neutron detection efficiency. The integrals over energy windows corresponding to the TOF windows can be compared with fluences calculated in part 9 to test the reliability of the evaluation process. A comparison of these spectra with those unfolded from the corresponding PH spectra (content of the next section) is a test of the particular unfolding procedure applied and a "negative" test of the calibration procedure in the following sense. An agreement between the spectral fluences resulting from unfolding and TOF analysis does not finally prove that the response matrix is correct, because for both the response matrix generation and the efficiency calculation the same algorithm and input data (codes NRESP7 and NEFF7) were used. But possible differences may show the influence of discrepancies between measured and calculated responses already mentioned.

The evaluation of the TOF spectra was performed separately (by means of the SPEKT code) for LGR and HGR in three steps:

- correction of the TOF spectra for "satellites";
- TOF → neutron energy scale conversion;
- division of the converted spectra by the neutron detection efficiency.

11.1. Correction of TOF spectra for "satellites"

The natural pulse sequence of the cyclotron is several times greater than the selected repetition frequency for the TOF measurement. Neutrons are also produced by cyclotron pulses that did not coincide with the selection frequency and were not fully suppressed; these are called satellites. They produce the same neutron spectrum as the others but they originate from pulses which have no corresponding pick-up pulses. Spurious peaks therefore appear in the TOF spectrum in strange places - e.g.near channel 240

https://doi.org/10.7795/130.20231025

in Fig. 7 (peaks between break-up region and the (d,n) peak are caused by the reactions of deuterons on oxygen and carbon on the gold target backing and the Mo entrance foil). The break-up region of a satellite spectrum is usually almost hidden in the same region of the spectrum of neutrons with the correct timing (it will be called the ordinary spectrum in this paragraph). When the timing is wrong the satellite neutrons do not appear in the PH spectra corresponding to the TOF windows (K9-K14), but they do appear in the entire PH spectrum (K7). To get the right neutron spectrum for both shape and amplitude we have to move the satellite neutrons to the right position. The correction procedure contained the following steps:

- The ratio of areas R_s of the satellite and the ordinary spectrum (d,n) peaks and their distance were calculated.
- The measured TOF spectrum multiplied by R_s and shifted by this distance was taken as the satellite spectrum. This spectrum was subtracted from the measured one.
- As the (d,n) peaks were not exactly the same in shape (double-peak shape for satellites follows from the method of their suppression), some small oscillations appeared at the satellite peak position after the subtraction. These oscillations were smoothed.
- To return to the original number of detected neutrons, the spectrum resulting from the last step was multiplied by $1+R_s$. This correction amounts to 0.73 % for the 11 MeV HGR and 12 % for the 16 MeV LG run. Values are given in Tab.15.

Except for the 12 MeV run only one satellite with the (d,n) peak in the TAC range appeared in the measured spectrum, and the procedure described was applied to all these spectra[13]. Beside

---

[13] The 12_MeV run spectra was just cleared of satellite peaks by a linear interpolation between values on both sides of the peak and because of the number and position of the satellite peaks (three peaks completely out of the ordinary break-up region).

https://doi.org/10.7795/130.20231025

satellites seen in TOF spectrum there are satellites out of TOF-TAC range which (d,n) peak cannot be seen but corresponding pulses are present in PH spectra. The correction for these satellites was not performed but is suggested in Appendix 4.

11.2. TOF → neutron energy scale conversion;

The conversion from TOF to neutron energy scale is straightforward and was performed by the TGZ command of the SPEKT code taking into account relativistic kinematics.

11.3. The neutron detection efficiency.

The neutron energy spectrum resulting from the previous step must be divided by the neutron detection efficiency[14] to get the spectral neutron fluence. The shape of the efficiency function depends on the detector threshold used - see Fig 13. To find the threshold, the corresponding PH spectra were differentiated by means of DIFF command of the SPEKT code using smoothing over 5 channels. The position of the center of gravity of the peak in the derivative was taken as the threshold in the NEFF7 code used for efficiency calculations and its variance can be taken as the threshold uncertainty. Both values are given in Tab. 13:

To estimate the uncertainty of integrals over the converted neutron spectrum we studied the sensitivity of it to the threshold position. Changing the threshold x-times, one gets a partial integral of the spectrum changed k_s*x-times and the sensitivity coefficient k_s ranges from 1.1 for 10 MeV LGR to 0.95 for 15 MeV LGR for the integral 2.-4.9 MeV which is the overlapping part of TOF spectra for both runs. In the case of HGR, the sensitivity is smaller: 0.77÷0.97. The (d,n) peak region of the LGR spectra shows

---

[14] The NEFF code calculates the efficiency of the given scintillator and the geometrical arrangement. To get comparable results i.e. fluence per cm^2 at the detector center, the efficiency was multiplied by the ratio of solid angles subtended by the scintillator and by a 1 cm^2 circle in the same position. The ratio was 20.1942.

https://doi.org/10.7795/130.20231025

a similar sensitivity (about 0.95). Combining the above values we get the extreme cases of a contribution to the neutron spectrum uncertainty due to threshold: for the integral over 2.-4.9 MeV it is about 10 % for 11 MeV HGR and about 2.3 % for the (d,n) peak integral of the 10 MeV LGR spectrum. The influence of the threshold on the spectrum shape is therefore mainly concentrated to the break-up region (see Fig.24).

Tab. 13: "Hardware" thresholds of "total" PH spectra (K7) and their variances.

run [MeV]	10	11	12	13	14	15	16
	low gain runs						
threshold [l.u.*10^3]	489.6	305.4	482.6	286.1	490.8	277.1	490.5
variance [%]	2.5	4.9	3.5	4.3	3.0	4.3	3.0
	high gain runs						
threshold [l.u.*10^3]	73.66	73.70	74.18	73.88	76.19	71.53	
variance [%]	5.8	10.6	6.9	10.5	6.9	9.8	

In chapter 9 we noted that the NRESP7 calculated response overestimates the measured one in the region where reactions on carbon took place (i.e. for neutron energies ≥ 10MeV), therefore the efficiencies must be corrected for this effect. They were multiplied by a function which is a linear fit of points in Tab.14. The values there are values of $\tilde{r}_i^{E/C}$ (see eq.(14) and Figs.20 & 21) where i is the threshold of the corresponding PH spectrum.

Tab.14: Correction of NRESP7 overestimate of the response for neutron energies > 10MeV at lower amplitudes (no correction performed below 10MeV).

energy [MeV]	10	11	12	13	14	15	16
correction [1]	1.0002	0.9987	0.9935	0.9774	0.9699	0.9581	0.9373

https://doi.org/10.7795/130.20231025

11.4. Comparison of (d,n) peak fluences.

The neutron spectra obtained separately for both gains were combined with this procedure to get the combined neutron spectrum. The overlapping region is from 2. to 4.9 MeV. Differences in integrals over the overlapping region are listed in Tab. 16. As with the PH spectra, neutrons are missing in the LGR TOF data. Nevertheless the spectra were combined using the HGR spectrum up to 4.9 MeV and the LGR spectrum above, without any additional renormalization.

The converted TOF spectra and their integrals are compared with the results of unfolded spectra in the following section. The integral over the (d,n) peak window[15] with the fluence calculation (part 9) is compared in Tab. 15 and again in Tab. 17. Satellites do not contribute to the spectra in K9[16] from which the fluence in 4-th column is calculated. Therefore the content should correspond to the non-corrected TOF spectrum, and the difference in evaluated

Tab. 15: Comparison of integral over the TOF window with fluence calculation (diff. means difference between these two quantities). "Sat.corr" means correction for satelites inside TAC range(see 11.1)

run	TOF window		fluence	peak int.	diff.	sat.corr
[MeV]	[MeV]		[$10^{-3}cm^{-2}$]		[%]	[%]
10	9.03	10.45	172.204	177.8	3.1	3.7
11	9.61	10.61	191.250	192.0	0.03	1.0
12	10.85	12.75	188.139	200.0	5.9	6.1
13	11.78	13.94	201.772	203.1	0.7	1.2
14	12.32	14.64	205.136	209.3	2.0	1.5
15	13.07	15.62	123.347	126.9	2.8	4.0
16	13.97	17.61	106.082	118.0	10.1	12.0

fluences must be be equal to the satellite correction. From Tab. 17 it is apparent that TOF method confirmed results from section

---

15 Range of TOF window in MeV was calculated by NEUTOF code from the range of the windows in channels (tab. 8) and calibration quantities in tab.7.

16 Only events with TOF pulses pertaining to the TOF window are recorded in K9.

https://doi.org/10.7795/130.20231025

11 up to 0.7 %.

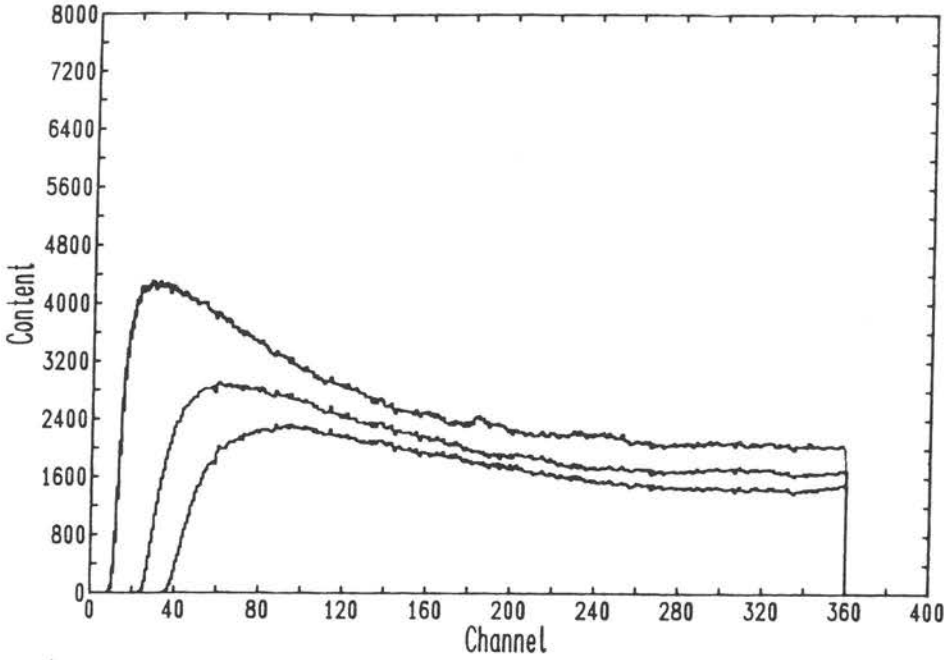

Fig.23:Efficiency of the IRD detector for different thresholds;
10 & 15 MeV L&HGR, scale is 20 channels/MeV.

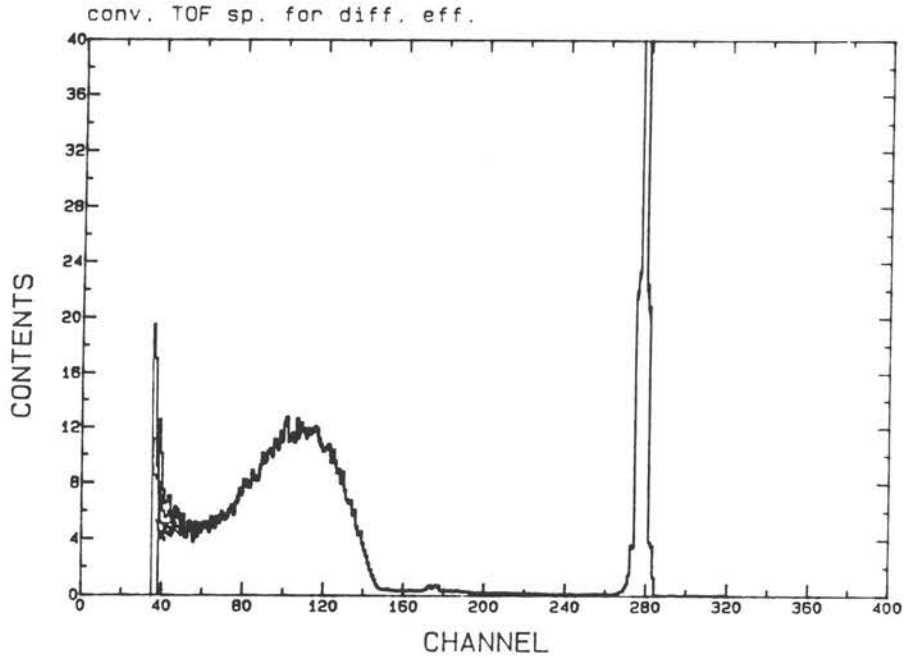

Fig. 24: TOF converted 14 MeV run spectra evaluated with
efficiencies calculated for various thresholds.

https://doi.org/10.7795/130.20231025

12. Unfolding of the pulse-height spectra

For each run from 10 to 16 MeV the following spectra were unfolded

- entire PH spectrum (K7),
- PH spectrum corresponding to (d,n) peak TOF window (K9) and
- PH spectrum corresponding mainly to the break-up region, i.e. the difference in the above spectra.

The results corresponding to the second and third case were added and the approach is referred to as unfolding per partes. The code DIFBAS [Ti-2-90] was used for the unfolding.

12.1. Input data for unfolding.

Prior to interfacing to the unfolding code, the PH spectra measured separately for LGR and HGR were combined (all except the 16 MeV run where only an LGR was performed). The difference already mentioned between the integrals of overlapping parts of LGR and HGR PH spectra corresponding to all TOF windows from K9 to K14 was confirmed when combining the entire spectra (K7). The differences are comparable with those in Tab. 11 (see Tab 16):

Tab. 16: Differences in % of overlaping integrals for LGR & HGR for the total PH und TOF spectra. The overlap ranges for PH spectra from 0.429 l.u. (1.681 MeV) for 11, 13, and 15 MeV runs and from 0.562 l.u. (2.031 MeV) for other runs to 14.827 MeV. The TOF spectra are compared in overlap from 2. to 4.9 MeV (MeV means neutron energy).

diff.[%] L/H gain runs	run [MeV]					
	10	11	12	13	14	15
PH spectra	-3.9	-1.9	-4.1	-2.6	-1.1	-3.6
TOF spectra	-6.4	-1.2	-3.7	-4.4	-0.9	-4.4

The combined PH spectra equal to the HGR spectrum below 1.966 l.u. (4.827 MeV) and to LGR spectrum for higher energies.

The code SPH developed for the following procedure is an

https://doi.org/10.7795/130.20231025

interface between the SPEKT code used for the evaluation of measured spectra and for the subtraction of K7 and K9 in this case, and the unfolding code DIFBAS. The light output scale given by the gain G established by γ-calibration was added to the PH spectra. These spectra were rebinned to the response matrix scale and the standard deviation equal to the square root of the channel contents was added as the uncertainty. No correlations of PH spectra were assumed.

Three possibilities were selected for an a priori neutron spectrum : constant function, the first derivative of the PH spectrum and TOF converted spectrum.

Considerable effort was devoted to the search for an optimum of the rest of input data - the a priori spectrum covariance matrix which is made up here of variation coefficients and correlations. For the constant a priori spectrum the variation coefficients were set equal to 10 % in the break-up and then slowly declined to 5 % in the interval between the break-up and the (d,n) peak where values of 100 % and 1000 % were used. For the other a priori spectra, values of 2 and 10 % were used over the whole spectrum range.

Gaussian correlations were generated by means of the algorithm used in the DIFBAS code [Ti-2-90]. The Gaussian width is related to FWHM and the two following FWHM formulas were used:

- the formula (1-3) where light output was exchanged for energy (parameters A=1., B=12. and C=25. were taken from a figure similar to Fig 18) and
- constant FWHM = 700 keV.

12.2. Discussion and conclusions.

The spectra unfolded with different input data were compared between one another and with converted and normalized TOF spectra on graphs. To get a numerical comparison, the integral over the whole range (total integral) and integrals over the break-up

https://doi.org/10.7795/130.20231025

region, valley and (d,n) peak, (partial integrals) were also compared. The limits of these parts were deduced from the shape (see Tab 18): The comparison begins at about 1 MeV (the TOF branch threshold) and the break-up part ranges from here to the point where the spectrum falls to almost zero (from 3.5 to 9 MeV for different runs). The area of the (d,n) peak was taken broader than the corresponding TOF window; it begins at the start of a "tail" (this will be explained later) and ends 1 MeV higher than the mean energy of the peak. The valley is the interval between these two parts (see Tab. 18).

The first conclusions were drawn from the unfolding of the entire PH spectra concerning the a priori spectrum selection:

- The first choice of the a priori spectrum - a constant function - results in an unfolded spectrum with the lowest influence of an a priori information (the situation of unknown spectrum unfolding is modelled). The position of both main parts, the break-up and the (d,n) peak, is supplied by values of a priori variance coefficients generally representing an expected change. This information seems to be enough to obtain satisfactory results and therefore most attention was devoted to the unfolding using this approximation and the results were used for the comparison with TOF spectra.
- The unfolding using the first derivative was performed for a few spectra only. The number of neutrons in the break-up part of the first derivative of the PH spectrum is overestimated (compared with the TOF spectrum) because reactions on carbon are not taken into account (see Fig. 25). Moreover, the (d,n) peak is broadened as a result of a necessary smoothing in the derivative procedure. In the unfolded spectrum, the first failure is corrected but to get the (d,n) peak width comparable with the correct value (calculated from kinematics) more information must be

https://doi.org/10.7795/130.20231025

added[17] or another procedure[18] must be used. This approximation therefore has no major advantage compared with the constant distribution.

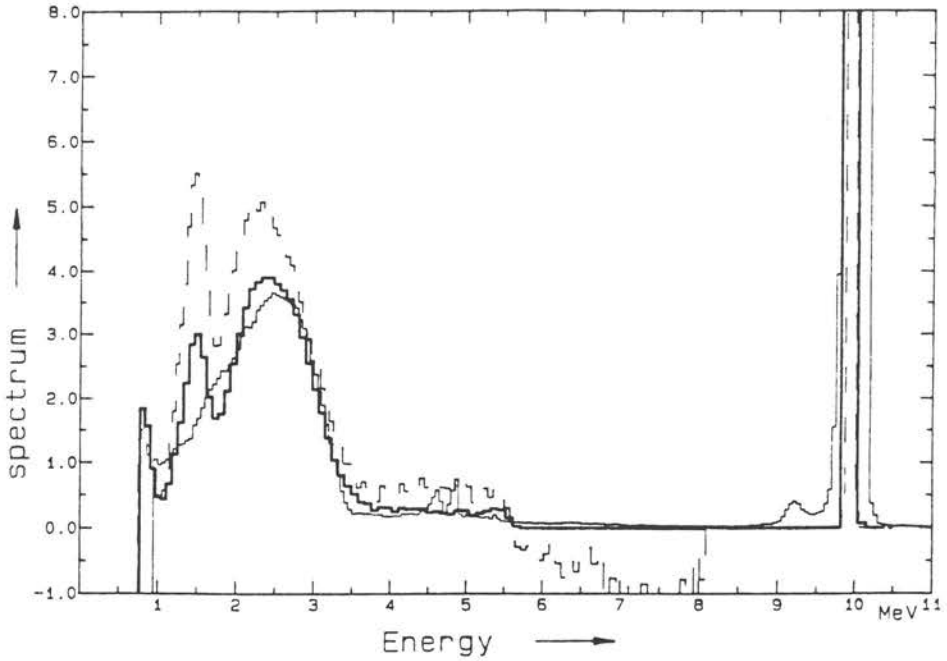

Fig.25: Comparison of spectra from the 10 MeV run: — TOF spectrum, ... 1. derivative of PH spectrum, ▬ unfolded spectrum (1. derivative with "thinned" (d,n) peak was used as an a priori spectrum).

- The third possibility - utilizing TOF spectra as a priori information was performed only to check the consistency of the spectrum evaluation methods. The two following conclusions were drawn (see Fig. 26):

---

17 This information can be for example included in function of the a priori variance used for a constant a priori spectrum.

18 SAND II modified [Ma-90] algorithm was used to remove the detector resolution and the broadening due to inevitable smoothing introduced by the derivative procedure. The "response matrix" was in this case a matrix generated by the same procedure as that used for the response folding in part 10. To get the optimum results the value of FWHM evaluated in part 4 had to be multiplied by 1.5 This coefficient was found by the "trial and error" method and the algorithms was rather sensitive to that value.

https://doi.org/10.7795/130.20231025

- The unfolded spectrum confirmed the spectral shape of the (d,n) peak including the small peak in the valley (see part 11). This peak probably caused by reactions of deuterons on oxygen and carbon cannot be unfolded using a constant a priori neutron spectrum.
- If partial and the total integrals of the TOF and the unfolded spectra are rather different (16 MeV run), the integrals of the spectrum unfolded with the TOF a priori information are nearer to those of the spectrum unfolded with the constant a priori spectrum than to the TOF spectrum itself.

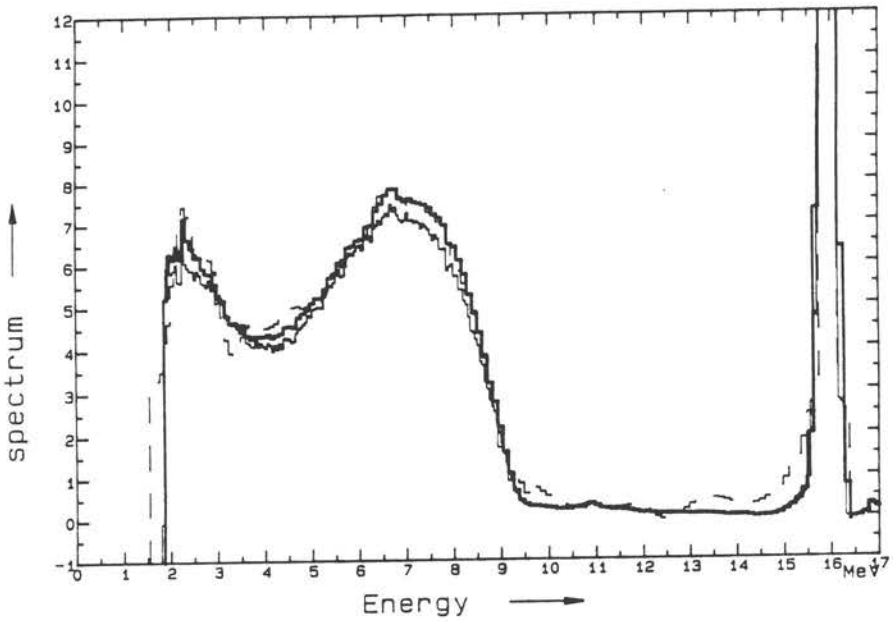

Fig.26: Comparison of 16 MeV run spectra: —— TOF spectrum,
..... unfolded spectrum with a constant apriori spectrum,
▬▬ unfolded with the TOF spectrum as apriori information.

While for a derivative and TOF a priori spectrum the set-up of input data there is almost without free choice, we can influence the results using the constant a priori spectrum. The influence on the integrals (total and partial) is small; in any case it did not exceed 2 % as presented in Tab. 18. However, the influence on the spectrum shape is greater; the following points summarizes conclusions from tests:

https://doi.org/10.7795/130.20231025

- A priori variation coefficients have a greater influence on the shape of the a posteriori spectrum than the correlations. The setting-up of the variation coefficient function of energy carrying the information on the expected spectrum shape is a rather sensitive task. But in the case when the variation coefficient function was wrongly set, dips to negative values appeared in the output spectrum. These usually disappeared if correct values were set; if they remained, e.g. at the lower part of the break-up where variation coefficient is constant, then it is clear that it is not due to the input data setting (see Fig. 27).
- The width of the (d,n) peak in the unfolded spectrum strongly depends on the range of high values of the variation coefficients and on the value itself (100 and 1000 % were tested). If the range is shifted or too narrow, dips appeared. Generally an increase in the value makes the peak narrower and a too broad

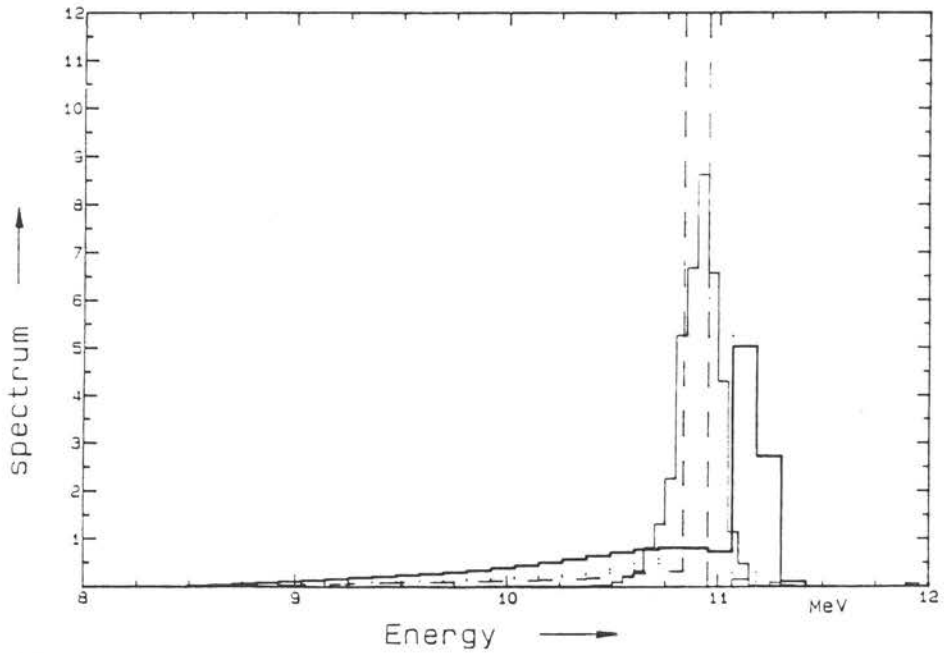

Fig 27: Comparison of 11 MeV run spectra using a constant a priori spectrum with TOF spectrum (—); ... & -- var. coef.= 100 & 1000 %, — intentionally wrong position of the peak.

range has the opposite effect. But for about a half the runs, application of the higher value (1000 %), which corresponds bet-

https://doi.org/10.7795/130.20231025

ter to the real change of the spectrum, was not successful as a result of the deep dips mentioned.

12.3. Comparison with TOF spectrum

The first comparable value is the fluence in the TOF window covering the (d,n) peak. This value was obtained by three different methods:

- The calculated responses were fitted to the measured ones as described in part 11; values are presented in Tabs. 12 and 15.
- The TOF spectra were integrated over the window; values in Tab. 15 must be decreased by satellite correction (no satellites are in the PH spectrum corresponding to the window).
- The unfolded PH spectra (K9) were integrated over the peak (the method is described in detail in section 12.4).

The differences are compared in Tab. 17.

Tab. 17: Differences of fluences in % over the (d,n) peak TOF window gained by integration of the TOF (Φ^{TOF}) and unfolded (Φ^{unf}) spectra from those Φ^{fl} gained in part 11.

diff.[%]	run [MeV]						
	10	11	12	13	14	15	16
$\frac{\Phi^{TOF} - \Phi^{fl}}{\Phi^{fl}}$	-0.4	-0.6	+0.2	-0.5	+0.5	-1.1	-0.7
$\frac{\Phi^{unf} - \Phi^{fl}}{\Phi^{fl}}$	-1.6	-2.1	-3.7	-3.1	-2.4	-2.2	-4.7

The differences $(\Phi^{TOF}-\Phi^{fl})/\Phi^{fl}$ are below the uncertainty of both methods. The differences in the second row are higher, but only part of this (about 1%) is caused by the inability of the unfolding code to completely suppress the flux below the peak where no neutrons are present due to TOF selection.

The comparison of the partial and the total integrals of entire unfolded PH spectra and TOF spectra is summarized in Tab 18.

From this table it can be concluded that:

▸ Except for the 16 MeV run the maximum of difference of the total

https://doi.org/10.7795/130.20231025

integrals is less then 3 %.

- The large differences of both signs in the integral in the valley region document a limited ability to reliably unfold the low fluence part.
- All differences in the total integrals and many partial ones are positive. But only the difference in the 16 MeV run seems to be significantly high to state that the PH spectrum contains more events than the TOF one and to cast doubts on satellite correction.

The shape of the entire unfolded spectrum (K7) using the constant a priori function differs from the TOF spectrum in two points remarkable in Figs. 25, 26, 28:

- Several artificial peaks and dips not present in the TOF spectrum appeared in the lower part of the break-up region (see Fig. 25). They can be removed only partially and only in some runs by an increase in correlations there.
- The (d,n) peak in the unfolded spectrum always has a "tail" towards lower energies (see Figs 26÷28). Its length and size depend on the energy of the (d,n) neutrons and can be slightly influenced by the range of the high value of the a priori variation coefficient. This effect is most pronounced in the 12 MeV LGR run.

In order to understand the first difference, the *per partes* unfolding was carried out. This is described in the next section.

The asymmetry of the (d,n) peak in the unfolded spectra - the "tail" - is remarkable mainly in Fig. 29. Its size can be characterized by the difference of the spectrum integrals over the TOF window and over the peak range used in Tab. 18. It is about 0.2÷0.7 % for TOF spectra and 10 times larger for the unfolded spectra. The existence of the "tail" can be explained by the difference between measured and calculated responses in the range between the response edge and the "second edge" (see part 5) and

https://doi.org/10.7795/130.20231025

Tab. 18: The differences [%] between unfolded PH spectra and TOF spectrum. Input data sets for unfolding were:

	a priori spectrum	var. coef. [%] at break-up	valley	peak	Gaussian correlations with FWHM given by
1.set	const	10 (8,6)	5	100	function eq.(5)
2.set	const	10 (8,6)	5	1000	FWHM=0.7 MeV
3.set	TOF	<---	2	---------->	function eq.(5)

Where implementation of the 2.data set was not successful, data are not presented; using the 3. data set, only the 12, 13 and 16 MeV run spectra were unfolded.

run	total	break-up	valley	peak	input data
10	2.2	3.3	11.0	1.5	1.set
MeV	2.7	5.1	-25.8	3.0	2.set
11	0.9	2.8	-15.4	0.3	1.set
MeV	1.1	3.4	-46.3	1.4	2.set
12	1.1	3.3	-13.3	-0.8	1.set
MeV	1.3	4.7	1.3	-2.6	3.set
13	0.8	1.5	16.2	-1.1	1.set
MeV	0.8	1.5	17.2	1.0	2.set
	1.8	3.1	1.9	-0.4	3.set
14	0.2	-0.4	39.6	-0.7	1.set
MeV	0.2	-0.1	22.6	-0.2	2.set
15	2.7	2.2	56.0	-0.3	1.set
16	6.4	6.0	33.3	4.2	1.set
MeV	6.1	6.3	3.3	5.9	3.set

Ranges [MeV] used for integration.

run	total	break-up	valley	peak
10 MeV	1.-11.	1.-3.5	3.5- 8.5	8.5-11.
11 MeV	1.-12.	1.-4.5	4.5- 8.8	8.8-12.
12 MeV	1.-13.	1.-5.5	5.5- 9.0	9.0-13.
13 MeV	1.-14.	1.-7.0	7.0-10.	10. -14.
14 MeV	1.-15	1.-7.5	7.5-10.5	10.5-15.
15 MeV	1.-16.	1.-8.0	8.0-12.	12. -16.
16 MeV	2.-17.	2.-9.0	9.0-13.5	13.5-17.

by weak a priori information (a constant function) used there in unfolding. When precise information about the spectrum in this range was supplied, the "tail" disappeared.

https://doi.org/10.7795/130.20231025

12.4. *Per partes* unfolding

If the PH spectrum corresponding to the break-up part only is unfolded, the influence of the neutrons having enough energy to produce α particles on carbon is strongly reduced. Discrepancies in the description of these reactions on carbon already mentioned in part 6 will not therefore have any influence on the unfolding, and the spectrum there should follow the smooth shape of the TOF spectrum. Indeed the peaks and dips did not appear in the spectrum unfolded from the PH difference spectrum (K7-K9), but when the peak unfolded spectra were added to that, 2 to 8 % of events were missing in the break-up range compared to the full-scale unfolding for 10÷13 MeV runs (e.g. 2.8 % for 13 MeV - see Fig.28). For 10÷12 MeV runs, the problem was solved by utilizing the first derivative instead of a constant as the a priori spectrum. But this a priori spectrum caused remarkable oscillations of the resulting spectrum in this region for 13 MeV and higher runs which were introduced by the derivative.

Another problem appeared in separate (d,n) peak unfolding. Up to 12 % (mainly for 15 & 16 MeV runs) of events were shifted from the peak range to lower energies (see Fig. 29) due to already mentioned discrepancies in the response matrix and the low weight of the peak region when a higher uncertainty was used there. A solution was found by introducing a "software threshold" of PH spectrum equal to the integration limit from Tab. 12 and using an artificial a priori spectrum equal to 1000 in the assumed (d,n) peak area[19] and to equal to 1 outside, together with 10 % uncertainty

---

19 From the above it can be deduced that the position of the (d,n) peak is a priori information necessary but usually unavailable for the unfolding. But the position of the peak maximum can be obtained from the first derivative, and the width by using "trial and error" method, as was done in section 12.2 for the position of the high uncertainty interval. We can get similar integral results using a constant a priori spectrum with a flat high (100%) uncertainty but the spectrum oscilles below the peak and the peak is broader.

https://doi.org/10.7795/130.20231025

all over the range.

Using the input data modifications mentioned the *per partes* unfolding results are in agreement with those from the full-scale unfolding as can be seen in Tab. 19. The test confirmed the confecture that artificial peaks and dips at energies below 3 MeV are not caused by the unfolding procedure but by the mentioned disagreement between measured and calculated responses.

Tab. 19: The difference [%] between total and partial integrals from full-scale and per partes unfolding.

	run [MeV]						
integral	10	11	12	13	14	15	16
total	+1.5	-1.2	-1.9	+2.2	-0.8	-0.7	-0.7
break-up	-0.3	-2.6	-2.9	-3.4	-0.5	-0.8	-0.3
peak	+1.8	-0.6	-1.8	-0.8	-1.2	+0.9	-0.7

12.5. Back-multiplication test.

To test the unfolding procedure and to explain the discrepancies between full-scale and *per partes* unfolding before the last modifications of the input data for the later approach, the following "back-multiplication test" was performed. The resulting spectra were multiplied by the response matrix, and integrals above the measurement threshold[20] of these "back multiplied" PH spectra and the measured PH spectra (input for the unfolding) were compared. The differences are given in Tab. 20. With the exception of four cases, the differences are lower than 1% which can be considered a rounding error limit. The differences for the sum spec-

[20] The measurement threshold (discrimination set on TSCA) is presented in Tab. 13. It was rounded to 0.09 l.u. for all combined spectra and to 0.5 l.u. for 16 MeV LGR. A higher threshold (a software threshold - see 12.4) was introduced to PH spectra before the unfolding of the (d,n) peak spectra (K9) employed for the comparison.

https://doi.org/10.7795/130.20231025

tra for 11 and 12 MeV runs, dragged there by the (d,n) peak unfolded spectrum, are caused by the disagreement between measured and calculated responses at low amplitudes already mentioned. They are not indicated in the last row because the integrals above the software threshold were compared. Other higher differences are in the break-up of 13 and 14 MeV runs. Neither a constant nor the 1st derivative a priori spectrum were suitable for the unfolding of the only break-up 13 MeV run spectrum. The difference (-3.4 %, see Tab. 19) is transformed into the -2.4 % here. The 14 MeV case is similar.

Tab 20: Differences between the "back multiplied" and measured spectra. The first column characterizes the unfolded spectrum which was multiplied by the response matrix. "1. & 2. set" mean the unfolded spectra with a constant a priori spectrum (see Tab. 18); "Sum" means per partes unfolded spectrum (sum of break-up and peak). The last two rows refer to unfolded spectra of break-up and (d,n) peak. The result of multiplication is compared in the first three rows with the total PH spectrum (K7); in the 5th and 6th rows with the difference PH spectrum (K7-K9) and with TOF window PH spectrum (K7).

unfolded spectrum	run [MeV]						
	10	11	12	13	14	15	16
1.set	- 0.2	- 0.3	- 0.2	- 0.1	- 0.1	- 0.1	+ 0.5
2.set	- 0.2	- 0.1		- 0.1	- 0.1		
sum	+ 0.1	- 2.5	- 2.0	- 0.6	+ 0.3	- 1.0	+ 0.4
break-up	- 0.1	- 0.8	< 0.1	- 2.4	- 1.6	- 1.2	- 0.4
peak	- 0.3	- 0.2	- 0.4	- 0.2	- 0.2	- 0.2	- 0.5

https://doi.org/10.7795/130.20231025

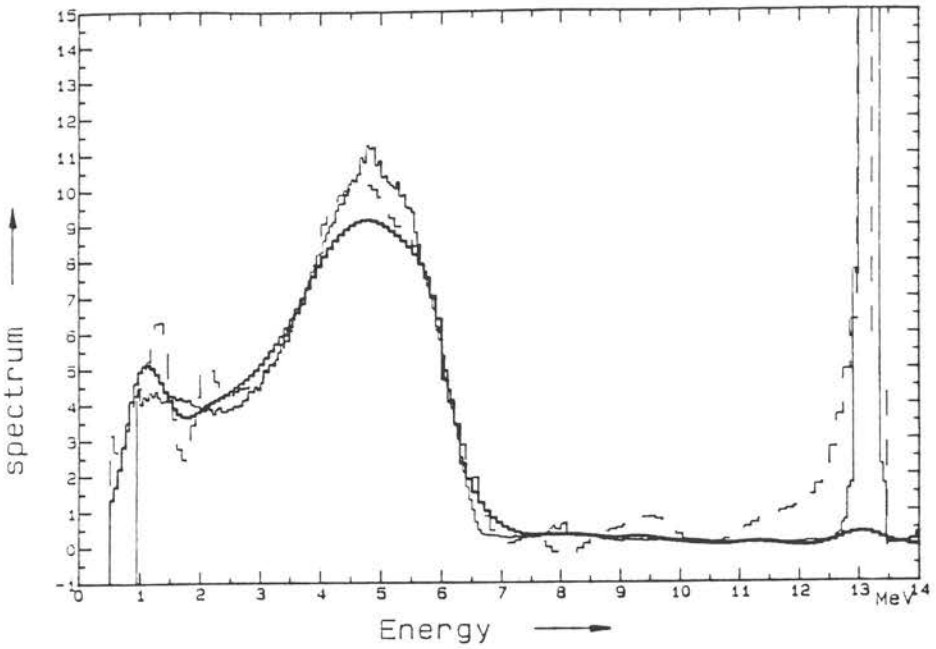

Fig 28: Comparison of 13 MeV spectra: — TOF spectrum, ... & ▬ total(K7) & break-up (K7-K9) unfolded spectra using a constant a priori function.

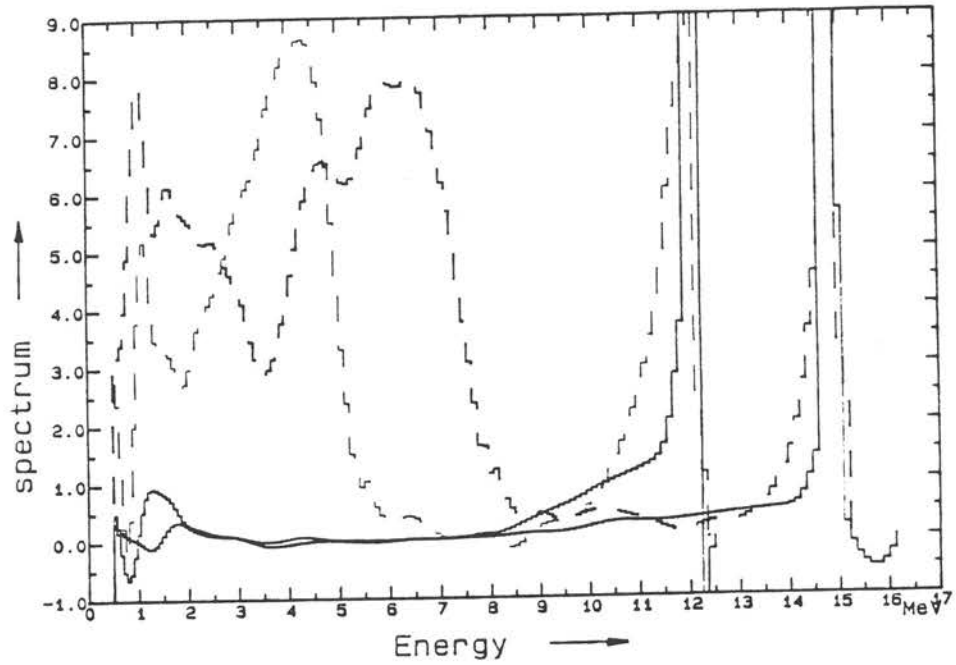

Fig.29: Shape of the unfolded spectra of the (d,n) peak at low energies and various shapes of the peak tail for total and per partes unfolding.

https://doi.org/10.7795/130.20231025

13. Conclusions

Performed first, the γ calibration established a connection of PH scales in channels defined by the ADC used to the instrument independent scale (in l.u.) based on assumed linearity of the light output for electrons. The estimated uncertainty of the coefficient (gain G) is about 0.4 % but when using it one should bear in mind that it was established by means of sources with Compton edges from 0.5 to 1.6 l.u., whereas the scale is used up to 10 l.u.. (The application of sources with higher energies was limited because of insufficiencies in the theoretical model (GRESP).)

The light output function for protons was specified by a simultaneous measurement of a neutron energy and the corresponding light output. The energy of neutrons produced in (d,n) and (d,np) reactions was measured by means of TOF technique, and the corresponding light output was evaluated in an iteration process comparing the measured and simulated PH spectrum corresponding to neutrons of the selected energy. The difference between the newly specified function and the function used so far for the scintillator under investigation (measured by Verbinski and in widespread use) is less than 9 %. It varies up to 4 l.u. and is almost constant (7±2%) above this. The uncertainty of the newly established function was estimated to be about 1%. A comparison of separate HGR and LGR measurements of edge positions in PH spectra confirmed the gain G specified in the γ calibration and in possible errors indicated: The amplification of HGR and LGR is changed by both high voltage and amplifier gain, and when this is reversed the amplification may differ by about 2-3 % even, if a great care is taken with the knob positions.

As a by-product of this procedure, the detector resolution function was specified for neutrons and photons. Values for both particles coincide.

The light output function for α particles used in NRESP7 was

https://doi.org/10.7795/130.20231025

only slightly changed (11 %) to fit the position of α peaks in PH measured and calculated spectra.

All spectra were normalized to monitor data. This normalization included dead-time corrections, which appeared to be a dubious matter thanks to a missing coincidence between EVENT and TOF signals. Two models for this purpose were applied and the second was chosen as the best one. Even these results were not satisfactory because almost systematic differences of about 2% in favor of HGR were found comparing integrals of overlapping parts of PH spectra measured separately for HGR and LGR. Wrong dead time correction or a wrong PS selection may be the reasons.

The HGR and LGR differences were confirmed when entire fluences were calculated comparing measured and calculated responses. We obtained an almost energy-independent difference of -3 % for the reference detector using values for HGR where available and LGR for higher energies (above 5 MeV).

Fluence values were confirmed by the integration of TOF spectra converted to neutron energy spectra; differences between the two methods were less than 1.2 % except in one case, but the TOF spectrum is not a fully independent method because the same algorithm is used for both efficiency and response calculations. The calculation of the detector efficiency appeared to be a very sensitive task if the threshold was not set by DAS software. Its a posteriori set has a rather large uncertainty which results in an uncertainty of the converted neutron spectrum. The second source of the spectrum uncertainty is that the estimation of "satellite" neutrons resulted in deuteron pulses with the wrong timing. This problem was only approximately solved.

The response matrix was calculated with the NRESP7 code using the light output function specified for 183 energies from 0.5 to 20 MeV. When it was rebined and folded by a Gaussian strip matrix we obtained a 256 * 183 response matrix which was used for unfolding of the measured PH spectra. The unfolding was performed by

https://doi.org/10.7795/130.20231025

means of the DIFBAS code using artificially-generated Gaussian correlations. A comparison with spectra obtained with the TOF method showed differences of less than 3 % of the total integral but always in favor of the unfolded spectra, which indicates an inadequate correction of satellite contribution. This comparison also confirmed the suspicion that the reactions on carbon within the detector as taken into account in the NRESP7 code are not correctly described, and this causes artificial peaks in the unfolded spectrum in the 1-3 MeV range.

The measurement was performed using the data acquisition and evaluation system of Neutron Metrology Group of the PTB. Several smaller codes were developed to support it and to interface it to the NRESP7 and DIFBAS codes. A description is given in the appendix.

https://doi.org/10.7795/130.20231025

References

[Bo-87] Boerker G.: Measurements of the Differential Neutron Scattering Cross Sections of Oxygen between 6 and 15 MeV, Thesis, Bochum 1987 (in German)

[Bo-88] Boerker G. et al: The Differential Neutron Scattering Cross Sections of Oxygen between 6 and 15 MeV, in: Nuclear Data for Science and Technology, ed. Igarasi S., Saikon Publ. Comp., Tokyo 1988

[Br-80] Brede H.J.et al: The Braunschweig Accelerator Facility for Fast Neutron Research, I. Building Design and Accelerators Nucl. Instr. & Meth. 169,1980,349

[Bu-65] Burrus W.R.: Utilization of A Priori Information by means of Mathematical Programming in the Statistical Interpretaion of Measured Distributions, Thesis, ORNL-3743, Oak Ridge (1965).

[Ca-90] Cabral S., Börker G.,Klein H., Mannhart W.: Neutron Production from the Deuteron Breakup Reaction on Deuterium, Nucl. Sci. & Eng. 106,1990,308

[Di-78] Dietze G.: SPEKT - A Dialog Program for Multichannel Spectra Analysis, PTB-ND-13, June 1978.
Schuhmacher H.:Manual for VAX-SPEKT

[Di-1-82] Dietze G., Klein H.: NRESP4 and NEFF4 Monte Carlo Codes for the Calculation OF Neutron Response Functions and Detection Efficiencies for NE 213 Scintillation Detectors, PTB-ND-22, Braunschweig, 1982

[Di-2-82] Dietze G., Klein H.:Gamma-calibration of NE-213 Scintillation Counters, Nucl. Instr. & Meth. 193,1982,549

[In-76] Ingersoll D.T., Wehring B.W., Johnson R.H.: Neutron Response Matrix for Unfolding NE-213 Measurements to 21 MeV, ORNL/RSIC-40, Oak Ridge 1976

[Jo-75] Johnson R.H.: A User's Manual for COOLC and FORIST,PNE-75-107, W. Lafayette (1975).

[Kl-80] Klein H. et al:The Braunschweig Accelerator Facility for Fast Neutron Research, II. Data Acquisition and Analysis, Nucl. Instr. & Meth. 169,1980,359

[Ma-85] Matzke M., Weise K.:Neutron Spectrum Unfolding by Monte Carlo unfolding, Nucl. Instr. & Meth. A234 (1985) 324

[Ma-90] Matzke M. et al: Transmission of Neutrons of 20 keV to 100 keV through Iron, Proceedings of Seventh ASTM-EURATOM Symposium on Reactor Dosimetry, Strasbourg, France, 27 - 31 August 1990, in print

[Pu-91] Pulpan J., Kralik M., Tichy M.: NE-213 neutron spectrometer for experiments with 14 MeV neutrons, Jaderna energie, 37,1991,141

[Sc-80] Schoelermann H., Klein H.: Optimizing the Energy Resolution of Scintillation Counters at High Energies, Nucl. Instr. & Meth. 169,1980,25

[Sh-80] Schlegel-Bickmann D. et al: A Collimator System for Fast

https://doi.org/10.7795/130.20231025

Neutron Scattering Experiments, Nucl. Instr. & Meth.
[Si-85] Siebert B.R.L., Brede H.J., Lesiecki H.: Corrections and Uncertainties for Neutron Fluence Measurements with Proton Recoil Telescopes in Anisotropic Fields, Nucl. Instr.& Meth. A235,1985,542
[Ti-88] Tichy M.: Bayesian Approach to Neutron Spectrum Adjustment, Nucl.Instr.& Meth. A267(1988)502.
[Ti-1-90] Tichy M., Kralik M., Pulpan J., Novotny T: Benchmark experiments with 14 MeV Neutrons Transmitted through Pb, Fe, Ni and Al,
Proceedings of Seventh ASTM-EURATOM Symposium on Reactor Dosimetry, Strasbourg, France, 27 - 31 August 1990, in print
[Ti-2-90] Tichy M.: Bayesian Unfolding of Pulse Height Spectra, Proceedings of Seventh ASTM-EURATOM Symposium on Reactor Dosimetry, Strasbourg, France, 27 - 31 August 1990, in print
169,1980,517
[Ve-68] Verbinski V.,V. et al.: Calibration of an organic scintillator for neutron spectrometry, Nucl.Instr.& Meth. 65,1968,8

https://doi.org/10.7795/130.20231025

Appendix 1. Detector electronics set-up.

```
PREA- 113-ORTEC scintilation preamplifier
        requir. voltage  ∓ 24 V  (17 mA)
        input capacity OUT

HV - 556- ORTEC          high voltage power supply
        VOLTAGE          *(1640 V / 1800 V)
        CONTROL          INT
        POLARITY         NEG

LA  - 572-ORTEC linear amplifier
        CORSE GAIN       *(100 / 200)
        GAIN             *(.69 / 1.00)
        SHAPING TIME     1 mikrosec.
        BLR              PZ ADJ.
        DELAY            OUT
        INPUT            POS

GBA - 444-ORTEC gated based amplifier
        CORSE GAIN       2
        GAIN             .6
        BLR              LOW
        BIAS LEVEL       0.
        MODE             NORMAL
        GATE             COINC           (R)
        STROBE           EXT             (R)

TFA - 474-ORTEC timing filter amplifier
        GAIN             *(1 / 1)
        FINE GAIN        *(1.division / 2.division)
        INTEGRATE        OUT
        DIFF             OUT
        INPUT            INV

CFD START - 1428A-CANBERRA constant fraction discriminator
        TRESHOLD         *(.30 / .15)
        MODE             CFSR
        DELAY            1.2 m of coax. cabel - 19 ns
        IN-OUT           OUT             (R)
        output signal delayed 56 ns by coax. cable


CFD START - 1428A-CANBERRA constant fraction discriminator
        TRESHOLD         *(.15)
        MODE             CFSR
        IN-OUT           OUT             (R)

DELAY - 2x NANOSECOND DELAY  CANBERRA 2058
        DELAY            72 nanosec.
```


https://doi.org/10.7795/130.20231025

TAC - 2143-CANBERRA time analyzer

GATE	ANT
STOP INHIBIT	OFF
DELAY	MIN
STROBE MODE	EXT
TIME RANGE	50 ns
DELTA T	10.00
TIME	0.00
SCA	OFF
STROBE WIDTH	16 μs
WIDTH TAC.SCA	1 μs (I)

TSCA - 551-ORTEC timing single channel analyzer

UPPER LEVEL	7.8 V	
LOW LEVEL	0.25 (0.15) V **	
MODE	NOR	
DELAY	0.1 μs	
LL	REF.	(R)
STROBE	INT	(R)

GDG - 416A-ORTEC gate & delay generator

DELAY	1.0
DELAY RANGE	0.1-1.1 μs
AMPLITUDE	5 V
WIDTH	3.5 μs

Note:
* means a value which is different for LGR and HGR. Values are presented: LGR/HGR.
** first value was used for all HGRs and for 10, 12, 16 MeV LGRs; then it was fot LGRs lowered to the value in brackets.
(R) means switch on the rear panel;
(I) means switch inside.

https://doi.org/10.7795/130.20231025

connected to the response matrix building, checking and using and to SPECT-DIFBAS interaction.

RMC code

The response functions for neutrons were calculated by the NRESP7 code. The code provides two output data sets (both are formatted ASCII files): the first one called RESULT contains integral parameters of calculated responses and it is determined for print. The second, named SPECT contains the response functions (both folded, unfolded and uncertainties). The size of the second one for for 183 responses is about 6 Mbyte. For reduction of this size, to check sequence of data and to separate folded and non-folded responses Response Matrix Conversion (RMC)Code was developed.

Control input file has the fixed name RMC.DAT and contains
1. filename of protocol file where data about the task are recorded;
2. filename of SPECT output file of NRESP7;
3. filename of RESULT output file of NRESP7;
4. filename of output file for non-folded responses (see part 10);
5. filename of output file for folded responses.

The code reads both NRESP7 files, checks the simultaneus sequence of responses, integral of the response and provides **two unformatted files** containing
1. basic input data for the detector and the generation case as in the SPECT file;
2. for each response:
   - sequence number, number of non-zero bins of the response, the mean neutron energy, the neutron energy group width and the integral over the response;
   - the non-folded resp. folded response for the first resp. second file (only contents of non-zero bins is recorded);
   - only for the second output file: the uncertainty of the folded response

MB code.

Matrix Building code reads non-folded response output file of RMC code and it is used for the following sequence of operations over a selcted range of neutron energies:
- Condensation of responses; problems with correlations are avoided by always combining k channels with an integer k=1,2,...,800 given as input parameter ICL.
- Folding responses by a gaussian matrix; this was described in the part 10 (it can skipped by setting all FWHM function parameters to zero).
- Writing a response matrix as unformatted direct access file.

https://doi.org/10.7795/130.20231025

Control input file has the fixed name MB.DAT and contains five records:

1. filename of "protocol file";
2. filename of RMC output file for non-folded responses;
3 filename of the response matrix to be built;
4. EMIN, EMAX thr range of neutron energy for which the response matrix has be built;
5. condensation factor ICL=k;
6. parameters of FHWM function a,b,c (for an exect meaning see part 5);

First output file - **protocol file** - contains the list of input data and the following information. Message "incomplete sum" tells that the renormalization of the folding matrix was performed acc. to eq. (R-10). Then one row is reporting about condensation and folding of each response: mean neutron energy neutron energy group width, number of non-zero bins of the response before and after condensation, after folding and error due to rounding errors in folding which was corrected to fullfil eq. (R-9).

The second output file is the **response matrix**. Columns of the matrix are responses e.i. PH spectra in l.u. scale. It means that each element of NRESP7 response is divided by width of PH bin. and to get a PH spectrum the matrix must be multiplied by neutron group fluences. Matrix is recorded row-wise to an unformatted file with direct access :

1.record:
NR,NC,IRL where
NR =M+M_{tail} is the number of the response matrix rows = number of the response bins after condensation+"tail" (see part 10);
NC is the number of columns i.e. number of neutron energy groups;
IRL is the record length of the file (note that unit in which parameter RECL is counted is different for VAX and PC computers).

2.+3.record :light output scale (edges of bins in l.u.):
2. record: EL(I),I=1,IRL
3. record: EL(I),I=IRL+1,NR+1

4.record: neutron spectrum energy scale (edges of groups in MeV)
EN(I),I=1,NC+1

5.- NR+4. record: row wise responses
RM(I,J),J=1,NC for I=1,NR

ATST code.

The ATST code is the first of three codes which enables access to a response matrix written as above. It prompts for the filename of the response matrix and a parameter NDIV (explanation later) and creates file ATST.PRI which is intended for print and it shows

- neutron energy scale
- light output scale
- maximum amplitude for each column of the response matrix

https://doi.org/10.7795/130.20231025

▸ non-zero elements of the matrix (marked by +).
Due to that width of a printer (usually <132) is smaller than number of response matrix collumns only each NDIV column is printed. NDIV should be approx. ≤ M/132 and the format no. 3 must agree with NC/NDIV.

EXTRF code.

EXTract Response Function code is able to extract the response function (collumn of the matrix) generated for the mean energy nearest to the chosen one to an unformatted file for a later utilization. The code prompts for the response matrix name, the energy for which the response is required and for the response output file. The structure of the unformatted output file is following:
1. record: number of light output intervals
 NR
2. record: light output scale
 VL(I),I=1,NR+1
3. record: required response function
 RF(I),I=1,NR

RMPOKE code.

Response Matrix POKE code enables to poke on a response matrix. A user is prompted for the filename of the response matrix and then for the number of the response matrix row and the starting and ending PH bin which will be typed together with the left edge of the corresponding neutron energy interval. For a special choice row no. -1 the light output scale is typed.

SPH code.

The SPH code makes an interface between SPEKT code and DIFBAS or FORIST (IRD version) codes. A formatted output file of the SPEKT code (ADT n,3,"filename" command) is read, can be rebined to the light output scale of the response matrix and written to an unformatted file required by the later mentioned codes. The code can be used for two purposes:
▸ Rebining of PH spectra to a PH scale of a response matrix (SPEKT file contains PH spectrum which is to be unfolded).
▸ An addition of an energy scale given by gain and channel number to a SPEKT file containing a neutron spectrum which should be used as an a priori spectrum or for another purpose (e.g. plotting).
The SPH code has an interactive input; an user is prompted for:
1. The response matrix name:
   -an actual filename is selected for the case of PH spectrun rebining;
   -"NO" is selected for the second case.

https://doi.org/10.7795/130.20231025

2. Gain in channels/l.u. (see γ calibration) and threshold channel in channels of the SPEKT file; this is first valid channel in PH spectrum and lower channels are ignored.
3. Two lines of comments which characterizes the PH spectrum - only in the case of PH spectrum rebining; they are printed by unfolding codes.
4. Output filename.

The output file has in the case of neutron spectrum structure of "IRD standard unformatted file":

1. record: number of energy intervals
 N
2. record: energy scale (edges of intervals)
 E(I),I=1,N+1
3. record: spectrum
 F(I),I=1,N

In the case of PH spectra rebining the output file has the structure of "PH spectra files" which is an extension of IRD standard unformatted file:

1. record: number of light output bins of the PH spectrum;
 number of the bin in the light output response matrix scale which is identical with the first bin of the PH spectrum,
 N,IS
2. record: light output scale (the same as light output scale of the response matrix starting with IS-th interval)
 VL(I),I=1,N+1
3. record: PH spectrum
 PH(I),I=1,N
4. record: response matrix filename (max. 30 characters)
 NAME (1:30)
5. record: comments (max. 160 characters)
 IDENT (1:160)

https://doi.org/10.7795/130.20231025

Appendix 3 List of all spectra and matrices recorded during the calibration.

All spectra contains 1024 channels; matrices have size 64*64 channels.

A. Spectra from monitoring detector (monitor)
K1 TOF spectrum, neutrons + photons;
K2 TOF spectrum, only neutrons;
K3 PH spectrum corresp. to TOF window over (d,n)peak, only neutrons;

B. Spectra from the studied detector without TOF windows ("entire"):
K4 PH spectrum, neutrons + photons;
K5 PS spectrum, neutrons + photons;
K6 TOF spectrum, neutrons + photons;
K7 PH spectrum, only neutrons;
K8 TOF spectrum, only neutrons.

C. Spectra from the studied detector corresponding to TOF windows (Tab 8); window 1 covers (d,n) peak, the other are in the break-up region:
K9 PH spectrum, only neutrons, window 1;
K10 PH spectrum, only neutrons, window 2;
K11 PH spectrum, only neutrons, window 3;
K12 PH spectrum, only neutrons, window 4;
K13 PH spectrum, only neutrons, window 5;
K14 PH spectrum, only neutrons, window 6;
K15 PH spectrum, only photons, window 1;
K16 PH spectrum, only photons, window 2;
K17 PH spectrum, only photons, window 3;
K18 PH spectrum, only photons, window 4;
K19 PH spectrum, only photons, window 5;
K20 PH spectrum, only photons, window 6;
K21 PH spectrum, only photons, window 7 (prompt γ peak);
K22 PH spectrum, only photons, window 8.

D. Matrices
K31 PH vers. PS matrix, neutrons + photons; monitor;
K35 PH vers. PS matrix, neutrons + photons, studied detector;
K39 PH vers. TOF matrix, only neutrons, studied detector;

https://doi.org/10.7795/130.20231025

Appendix 4 Clearing of "out of range" satellites

Each spectrum measured contained several satellites; some of them can be clearly identified in the spectrum when the corresponding (d,n) peak is inside the TAC range (800 ns). But the identification of satellites having (d,n) peak pulses in the gap between the TAC range and the next main pulse (1250 ns) is rather complicated. These events were not rejected by the IRD detection chain because there is no coincidence between TOF and EVENT=PS&PH branches (see Fig. 1). The break-up part of such a satellite appeared partially in the TOF spectrum as a flat background of the ordinary spectrum clearly visible to the right of the (d,n) peak. The "invisible" part measured rest is counted in channel 0 (ADC of TOF branch out of range) and in channels 3÷13, an amplitude corresponding to "DC zero" of this branch (no signal on TOF branch coincides with an EVENT signal). In the PH spectra these satellites are recorded with the correct amplitude, and the TOF spectrum must be corrected for comparison of TOF and unfolded spectra.

The TOF spectra were corrected for satellites for which the (d,n) peak appeared in the spectrum (as described). The corrections are listed in Tab.T2. In TOF-to-energy conversion procedure, "out-of-range satellites" were converted from the peaks at channels 0 and 3÷13 to a peak in an energy interval between 800 and 850 keV for 11 and 15 MeV runs, and between 900 and 950 keV for other runs (depending on the γ peak position). They were then simply cleared out by the SPH code. A ratio of the integrals over intervals where these satellites appeared (channels 0÷13 & above the (d,n) peak in TOF spectra before the conversion) to the ordinary spectrum range (from 13 to the end of the (d,n) peak) gives a rough idea of the corrections necessary . The ratio r^s and f^3 correction[21] is given in % in Tab.A3

---

[21] Correction f^3 which was calculated in part 8 but not used is similar to this one, but it was calculated as ratio of the sums

https://doi.org/10.7795/130.20231025

Tab.A3: Ratio of "hidden" peaks to the integral of spectrum and dead-time correction for the independent TOF branch.

correct.		run [MeV]						
		10	11	12	13	14	15	16
HGR	r^s	5.3	2.5	7.1	4.5	4.7	6.2	
	f^3	1.72	1.97	2.46	2.71	0.89	1.66	
LGR	r^s	2.3	0.8	3.6	1.2	0.9	2.4	7.6
	f^3	0.46	0.58	1.07	0.59	0.51	0.86	3.31

The following arguments can be used against application of this correction :

- The area between channel 0 and 13 does not necessarily contain only pulses with wrong timing i.e. satellites, but may also contain pulses belonging to an ordinary TOF spectrum if the TOF branch was "dead" and an event was recorded in the PH spectrum. The correction of the TOF spectrum for such pulses was already applied as the TOF "dead time" correction.
- Some of the "out-of-range" satellites are hidden, appearing as background over the ordinary spectrum range. The relative amount of this part may differ for corresponding LGR and HGR spectra, in which case application of the correction may be disproportionate (with respect to LGR & HGR).
- It is argueable whether the correction is correct when its application will increase the discrepancy between HGR and LGR.

0-13 to 13-1023 channels (the area above the (d,n) peak was added to the ordinary spectrum).

https://doi.org/10.7795/130.20231025

https://doi.org/10.7795/130.20231025